The Astronomical Journal, 170:98 (18pp), 2025 August https://doi.org/10.3847/1538-3881/ade1db

Predictions of the LSST Solar System Yield: Discovery Rates and Characterizations of Centaurs

Joseph Murtagh[1], Megan E. Schwamb[1], Stephanie R. Merritt[1], Pedro H. Bernardinelli[2,3], Jacob A. Kurlander[3], Samuel Cornwall[4], Mario Jurić[2,3], Grigori Fedorets[5,6], Matthew J. Holman[7], Siegfried Eggl[4,8], David Nesvorný[9], Kathryn Volk[10], R. Lynne Jones[11,12], Peter Yoachim[2,3], Joachim Moeyens[2,3,13], Jeremy Kubica[14,15], Drew Oldag[2,3,15], Maxine West[2,3,15], and Colin Orion Chandler[2,3,15]
[1] Astrophysics Research Centre, School of Mathematics and Physics, Queen's University Belfast, BT7 1NN, UK; jmurtagh05@qub.ac.uk
[2] DiRAC Institute, University of Washington, 3910 15th Ave. NE, Seattle, WA 98195, USA
[3] Department of Astronomy, University of Washington, 3910 15th Ave. NE, Seattle, WA 98195, USA
[4] Department of Aerospace Engineering, University of Illinois at Urbana-Champaign, 104 S. Wright St., Urbana, IL 61801, USA
[5] Finnish Centre for Astronomy with ESO, University of Turku, FI-20014 Turku, Finland
[6] Department of Physics, University of Helsinki, PO Box 64, 00014, Helsinki, Finland
[7] Center for Astrophysics | Harvard & Smithsonian, 60 Garden St., MS 51, Cambridge, MA 02138, USA
[8] Department of Astronomy, University of Illinois at Urbana-Champaign, 104 S. Wright St., Urbana, IL 61801, USA
[9] Department of Space Studies, Southwest Research Institute, 1301 Walnut St., Suite 400, Boulder, CO 80302, USA
[10] Planetary Science Institute, 1700 East Fort Lowell, Suite 106, Tucson, AZ 85719, USA
[11] Rubin Observatory, 950 N. Cherry Ave., Tucson, AZ 85719, USA
[12] Aston Carter, Suite 150, 4321 Still Creek Dr., Burnaby, BC V5C6S, Canada
[13] Asteroid Institute, a program of B612 Foundation, 20 Sunnyside Ave., STE F, Mill Valley, CA 94941, USA
[14] McWilliams Center for Cosmology, Department of Physics, Carnegie Mellon University, Pittsburgh, PA 15213, USA
[15] LSST Interdisciplinary Network for Collaboration and Computing Frameworks, 933 N. Cherry Ave., Tucson, AZ 85721, USA
Received 2024 December 20; revised 2025 May 29; accepted 2025 June 4; published 2025 July 21

Abstract

The Vera C. Rubin Observatory Legacy Survey of Space and Time (LSST) will start by the end of 2025 and operate for 10 yr, offering billions of observations of the southern night sky. One of its main science goals is to create an inventory of the solar system, allowing for a more detailed understanding of small-body populations, including the Centaurs, which will benefit from the survey's high cadence and depth. In this paper, we establish the first discovery limits for Centaurs throughout the LSST's decade-long operation using the best available dynamical models. Using the survey simulator `Sorcha`, we predict a roughly 7-fold increase in Centaurs in the Minor Planet Center (MPC) database, reaching ∼1200–2000 (dependent on definition) by the end of the survey—about 50% of which are expected within the first 2 yr. Approximately 30–50 Centaurs will be observed twice as frequently, as they fall within one of the LSST's Deep Drilling Fields (DDF) for on average only up to 2 months. Outside of the DDFs, Centaurs will receive ∼200 observations across the *ugrizy* filter range, facilitating searches for cometary-like activity through point-spread function extension analysis, as well as fitting light curves and phase curves for color determination. Regardless of definition, over 200 Centaurs will achieve high-quality color measurements across at least three filters in the LSST's six filters. These observations will also provide over 300 well-defined phase curves in the *griz* bands, improving absolute magnitude measurements to a precision of 0.2 mag.

Unified Astronomy Thesaurus concepts: Centaur group (215); Small Solar System bodies (1469); Sky surveys (1464)

1. Introduction

The Centaurs are a class of small, icy bodies that orbit the Sun on giant-planet-crossing paths. They are a transient population, evolving inward into the solar system from the trans-Neptunian population owing to frequent gravitational perturbations with the giant planets, leading to orbits with dynamical timescales on the order of ∼1–10 Myr (M. S. Tiscareno & R. Malhotra 2003; R. P. Di Sisto & A. Brunini 2007; K. Volk & R. Malhotra 2008; B. L. Bailey & R. Malhotra 2009; R. P. Di Sisto & N. L. Rossignoli 2020). Centaurs face a variety of fates from these interactions; some may have impacts with the giant planets, while some may be ejected out of the solar system entirely (L. Dones et al. 2015). Others still may diffuse inward from the trans-Neptunian region into the solar system to become short-period comets, such as the Jupiter-family comets (JFCs; M. J. Holman & J. Wisdom 1993; M. J. Duncan & H. F. Levison 1997; H. F. Levison & M. J. Duncan 1997; M. Duncan et al. 2004; V. V. Emel'yanenko et al. 2005; K. Volk & R. Malhotra 2008; D. Jewitt 2009; G. Sarid et al. 2019; A. Guilbert-Lepoutre et al. 2023). Further evidence of this evolutionary continuum is seen in the color distribution of known Centaurs following closely with that of the smaller-sized trans-Neptunian objects (TNOs; N. Peixinho et al. 2003; S. C. Tegler & W. Romanishin 2003; S. C. Tegler et al. 2008, 2016; W. C. Fraser & M. E. Brown 2012; N. Peixinho et al. 2012; I. Wong & M. E. Brown 2016, 2017), while also having a size distribution more similar to that of the JFCs (S. S. Sheppard et al. 2000; R. Jedicke et al. 2002; J. M. Bauer et al. 2013; Y. R. Fernández et al. 2013). Study of Centaur properties in ensemble is therefore a means of providing insight into the evolution of dynamically scattering TNOs into

present-day comets, as well as probing the evolution of how their surfaces are processed.

There is no unanimous definition of a Centaur in literature, with cuts being made in orbital space and/or in dynamical timescales (e.g., H. F. Levison & M. J. Duncan 1997; M. S. Tiscareno & R. Malhotra 2003; R. P. Di Sisto & A. Brunini 2007; D. Jewitt 2009; G. Sarid et al. 2019; N. Peixinho et al. 2020); however, the most common community consensus places their orbits between Jupiter and Neptune. It is due to this variety of definitional cuts, as well as the inherent dynamical instability that Centaurs display, that there is no consistent count of either the observed or intrinsic number of Centaurs. Recently, K. Volk & C. Van Laerhoven (2024) applied the B. Gladman et al. (2008) definition to all known multi-opposition outer solar system objects within the Minor Planet Center,[16] resulting in a list of 168 known Centaurs at the time of writing. The relatively small number of known Centaurs (compared to other TNO populations) is partly due to there having been a lack of dedicated Centaur discovery surveys (see J. A. Kurlander et al. 2025 for a survey of the Pan-STARRS1 detection catalog), with the majority being serendipitously discovered in other TNO, Main Belt asteroid, or near-Earth object searches (e.g., J. M. Petit et al. 2008; C. A. Trujillo 2008; S. S. Sheppard et al. 2011; D. Rabinowitz et al. 2012; E. R. Adams et al. 2014; S. S. Sheppard et al. 2016; R. J. Weryk et al. 2016; M. T. Bannister et al. 2018). Lack of follow-up observations or detection algorithms being designed for either slow or fast movers in these surveys means that the Centaurs, which by any definition cover a wide range of orbital space, are less preferentially observed. Their small inherent population size relative to the TNOs or asteroids adds to this issue of missing Centaur discoveries. A survey that probes this region of the outer solar system will thus be required to be designed to cover these gaps in observation space.

At the Vera C. Rubin Observatory in Chile, the Legacy Survey of Space and Time (LSST) is scheduled to begin survey operations by the end of 2025. With a 9.6 deg^2 field of view, one of the LSST's science goals will be cataloging the entire solar system (Ž. Ivezić et al. 2019). The LSST is set to revolutionize solar system study—with its cadence of 30 s exposures covering 18,000 deg^2 every three nights across six broadband *ugrizy* filters (LSST Science Collaboration et al. 2009; Ž. Ivezić et al. 2019; F. B. Bianco et al. 2022), the LSST has been uniquely tuned to give the best compromise of observing strategy across all small-body populations. Specific patches of the sky known as Deep Drilling Fields (DDFs) will be targeted with higher temporal cadences, allowing for observations at a stacked magnitude deeper than the main Wide-Fast-Deep (WFD) survey over 10 yr (F. B. Bianco et al. 2022), while minisurveys will be carried out in areas like the Northern Ecliptic Spur (NES, $+10^\circ$ ecliptic latitude), wherein additional *griz* observations in the ecliptic plane will allow for enhanced detections of outer solar system objects with longer orbital periods (M. E. Schwamb et al. 2023). All of these combined mean that over its planned 10 yr long observational baseline it has been predicted that the LSST will discover roughly an order of magnitude more objects in each small-body population residing in the solar system (R. L. Jones et al. 2009, 2018; LSST Science Collaboration et al. 2009; M. Solontoi et al. 2010; A. Shannon et al. 2015; T. Grav et al. 2016; K. Silsbee & S. Tremaine 2016; P. Vereš & S. R. Chesley 2017; R. L. Jones et al. 2018; Ž. Ivezić et al. 2019; G. Fedorets et al. 2020; D. J. Hoover et al. 2022). The LSST's deep, high-cadence observations will provide particular opportunities for investigations into the key areas of Centaur characteristics, including probing potential cometary activity and ring systems and developing quality phase curves, rotational light curves, and photometric colors (R. L. Jones et al. 2009; LSST Science Collaboration et al. 2009; M. E. Schwamb et al. 2018, 2021, 2023).

Despite its readily apparent strengths for Centaur discovery, there have been no estimates on the Centaur yield within the LSST. The recent cadence optimization work by M. E. Schwamb et al. (2023) specifically excludes the Centaur population in their simulations, as does the LSST Science Collaboration et al. (2009) analysis. Predictions for the Centaur discovery metrics, including the total number of observations available per object, when they are discovered, and how many will be discovered, are vitally important in understanding the potential for Centaur science within the LSST through light-curve, phase-curve, and surface-color studies. Further, such predictions for Centaur observations are crucial for understanding the gaps in the LSST's observation cadence, which will enable the design of follow-up observational campaigns to supplement and bolster the LSST, such as for investigating Centaur activity. In this work, we address this gap in planning for Centaur science within the LSST by providing the very first estimates of Centaur discovery metrics using the current best dynamical and physical models from literature.

In Section 2, we describe our methods of modeling discovery, using the survey simulator `Sorcha`, a solar system survey simulator, simulated LSST observation cadences, and a model for the Centaurs. In Section 3, we outline the results of these simulations, including discovery rates for Centaurs within the first few years of the LSST, potentials for Centaur activity probing, and phase-curve, light-curve, and surface-color metrics. Finally, Section 4 summarizes the major results of Centaur discovery and characterization within the LSST and also highlights the potential limitations to this work.

2. Methods

In this work we use the leading dynamical model from D. Nesvorný et al. (2019) of the Centaur population, calibrated to Centaur detections in the Outer Solar System Origins Survey (OSSOS; M. T. Bannister et al. 2018), in order to gain the first predictions for the number of Centaurs that will be discoverable within the LSST. From these predicted observations, we explore the analysis that is possible within both early and later years of operation of the LSST through the measurements of light curves, phase curves, color information, and any cometary-like activity. As the LSST is a well-characterized survey (i.e., its depth per observation, pointing histories, and detection efficiencies will be measured; see S. M. Lawler et al. 2018a for further discussion), we simulate what objects would be detected within the LSST and forward-bias them in order to estimate the number of LSST Centaur discoveries.

[16] https://minorplanetcenter.net/iau/lists/MPLists.html

2.1. Simulating with Sorcha

We simulate our Centaur discoveries within the LSST using `Sorcha` (M. J. Holman et al. 2025; S. R. Merritt et al. 2025), an open-source, modular, `Python` survey simulator designed with surveys such as the LSST in mind. We refer the reader to S. R. Merritt et al. (2025) for a full discussion on how `Sorcha` has been designed, but we highlight the basic functionality here for clarity. `Sorcha` takes an input model of the Centaurs, described by object orbital elements and physical parameters such as absolute magnitude in r band, photometric colors with respect to r, and the same phase-curve parameters in all bands (see Section 2.3). Ephemerides are generated for objects using the built-in N-body integrator ASSIST (M. J. Holman et al. 2023)—itself an extension of the REBOUND package (H. Rein & S. F. Liu 2012; H. Rein & D. S. Spiegel 2015), using its IAS15 integrator (Gauss–Radau integrator with adaptive step-size control, 15th order; H. Rein & D. S. Spiegel 2015) with the Sun, the Moon, the planets, and 16 massive asteroids and dwarf planets (see Table 5 in S. R. Merritt et al. 2025 for list) as perturbers. Given a database of the LSST's pointings (see Section 2.2), `Sorcha` computes whether the object is located within a $2.^{\circ}26$ radius of the pointing center and then applies the LSSTCam footprint (LSST Science Collaboration et al. 2009; Ž. Ivezić et al. 2019). For those objects that are not located within a gap in the CCD chips, a magnitude is calculated using the absolute magnitude (see Section 2.3.2) and the phase angle of the observation (see Section 2.3.4). Any sources brighter than $m_r = 16$ are removed, as they exceed the estimated saturation threshold of the LSST (Ž. Ivezić et al. 2019). The source detection efficiency is modeled for all observations by a modified sigmoid function from S. R. Chesley & P. Veres (2017) as follows:

$$\epsilon\left(m_{\mathrm{PSF}}\right) = \frac{F}{1 + e^{\frac{m_{\mathrm{PSF}} - m_{5\sigma}}{w}}}, \tag{1}$$

where $\epsilon(m_{\mathrm{PSF}})$ represents the probability of detection, F is the survey's peak detection efficiency, m_{PSF} and $m_{5\sigma}$ are respectively the object's point-spread function (PSF) magnitude (the source magnitude measured by the Rubin source detection algorithm; S. R. Merritt et al. 2025) and 5σ limiting magnitude of the observation at the source's location on the camera focal plane, and w is the width of the function. In this work we select $w = 0.1$, following the Sloan Digital Sky Survey (SDSS; J. Annis et al. 2014), and $F = 1$ (source detection for the LSST has already been well tuned for bright sources, and the true value is predicted to be close to 1; M. Jurić et al. 2021). Objects that have an apparent magnitude in the r band $m_r < 16$ are removed, as they are below the estimated saturation limit for the LSST (Ž. Ivezić et al. 2019). Finally, the LSST will also be the first survey at this scale with a dedicated moving object detection pipeline designed to search inward of Venus to beyond Neptune (Ž. Ivezić et al. 2019; M. Jurić et al. 2021). `Sorcha` models the Rubin Solar System Processing (SSP) object-linking algorithm, which will associate moving sources through the linking of three pairs of nightly observations (or tracklets) that are separated spatially by $>5''$ and temporally by <90 minutes, all within a 15-day window, with a design specification of 95% of discovery opportunities that meet these criteria being successfully linked (LSST Science Collaboration et al. 2009; Z. Ivezić & the LSST Science Collaboration 2013; J. Myers et al. 2013; Ž. Ivezić et al. 2019; M. Jurić et al. 2020). The resulting output from `Sorcha` contains predicted observations of all input objects that would be detectable in the LSST.

Simple magnitude and visibility cuts can approximate the number of detections per object but fail to capture the full complexity of a real survey. These cuts assume uniform observation conditions, which do not apply to the LSST's observing cadence. Using a survey simulator with ephemeris generation accounts for object motion and the ability to link detections across multiple visits. Additionally, the simulator can incorporate detection efficiency, allowing for the possibility of detecting objects fainter than the nominal survey magnitude limit through repeated observations. These effects are difficult or impossible to model accurately with simple cuts and require a survey simulator for realistic results.

2.2. The LSST Cadence Simulation

We use the output baseline cadence from v4.0 of the observing strategy (SCOC 2024) throughout all of our runs, with the number of visits across all filters shown in sky-map form in Figure 1. This simulation is generated by the `rubin_sim` package (F. B. Bianco et al. 2022; P. Yoachim et al. 2023) and the Rubin Observatory scheduler `rubin_scheduler` (E. Naghib et al. 2019; P. Yoachim et al. 2024).[17] It is based on a model observatory of the LSST that calculates on-sky limiting magnitudes and seeing conditions at each pointing based on assumed realistic weather conditions, telescope and camera performance, and individual filter responses with up-to-date mirror coating specifications (A. J. Connolly et al. 2014; F. Delgado et al. 2014; F. Delgado & M. A. Reuter 2016; P. Yoachim et al. 2016; LSST Science Collaboration et al. 2017; R. L. Jones et al. 2018, 2020; E. Naghib et al. 2019; F. B. Bianco et al. 2022). The most up-to-date observing cadence as determined by the Rubin Survey Cadence Optimization Committee (SCOC; SCOC 2022, 2023, 2024), including exposure time per filter and on-sky pointing position, is then applied, allowing simulated observations to be forward-biased to what the LSST will "see." Compared to prior cadence simulations, more time is spent on engineering downtime in year 1. This is, however, largely gained back in subsequent years and so only affects year 1 metrics. While this simulation starts in 2025 May, Rubin Operations have assumed a need for at minimum 6 weeks' worth of contingency and construction delay (L. P. Guy et al. 2024),[18] so true start dates will differ.

We note two different versions of this baseline—`one_snap_v4.0`, wherein the *grizy* observations are obtained in a single 29.2 s exposure (referred to as one-snap), and `baseline_v4.0` with 2 x 15 s exposures (referred to as two-snap). In either case, the u exposure is set at a single 38 s exposure (SCOC 2024). We focus in the main body of this work on the one-snap simulation, as the cadence recommendations are to move operations toward this as the feasibility of cosmic-ray rejection is tested during commissioning.

[17] For the most up-to-date cadence simulations, see https://s3df.slac.stanford.edu/data/rubin/sim-data/.

[18] See https://rubinobservatory.org/about/construction for the most recent timeline updates.

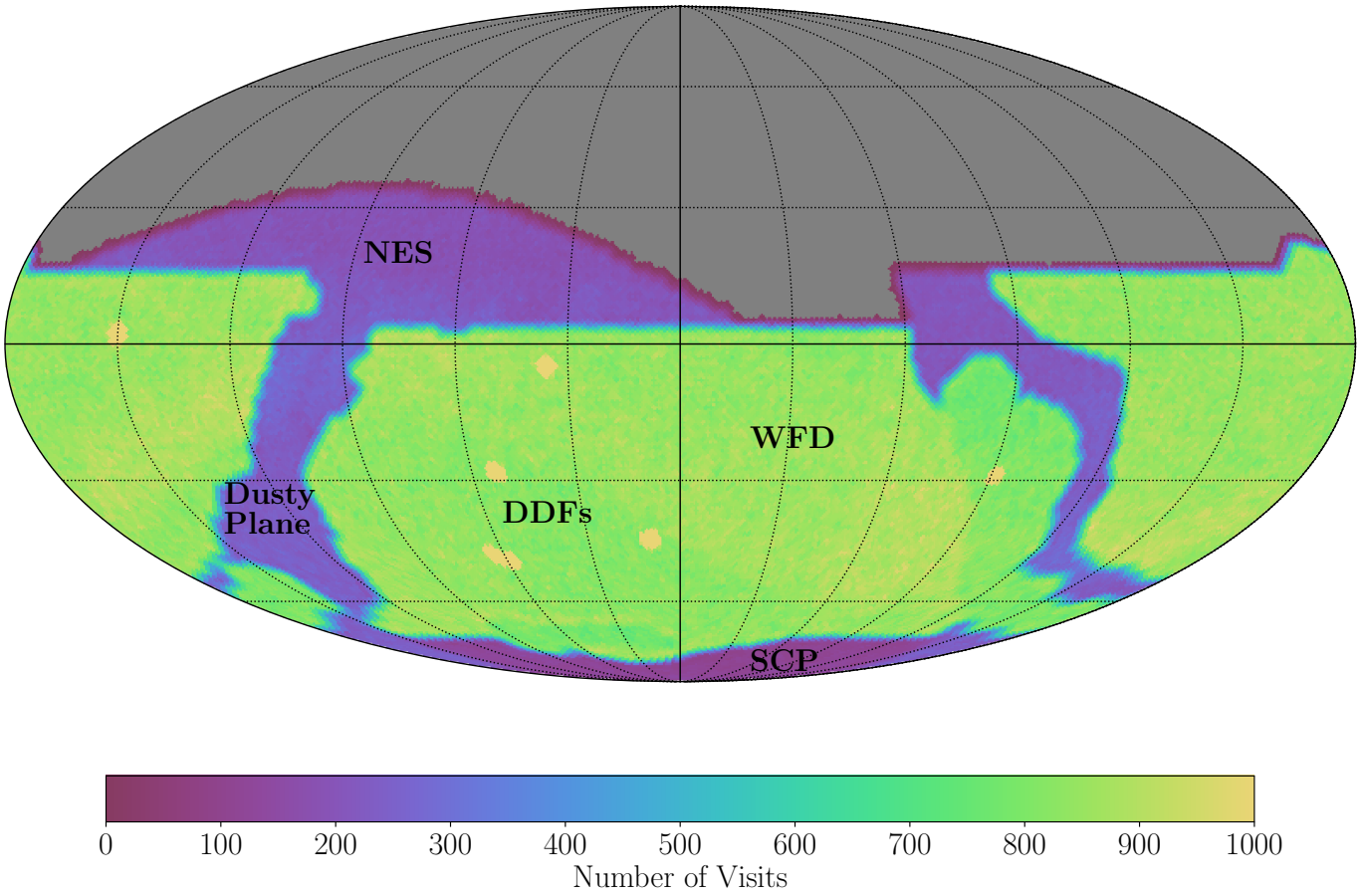

Figure 1. Sky map of the number of visits across all filters of the 10 yr LSST survey cadence based on the one snap v4.0 simulation (SCOC 2024). The main WFD survey making up ∼80% of the total survey time will receive ∼800 visits per pointing. There are additional "Mini" surveys highlighted that make up ∼3%–10% of the survey time. These cover differing areas of the sky, including the NES, the South Celestial Pole (SCP), and the Dusty Plane. Additionally highlighted are DDFs, regions within the WFD that will receive deeper coverage and more frequent temporal sampling and use a total of ∼6.5% of the survey time. For complete details of the survey strategy, see SCOC (2024).

2.3. Centaur Model

Initially we construct a Centaur model based on the dynamically driven definition from B. Gladman et al. (2008, hereafter G08), which makes cuts in perihelion distance $q > 7.35$ au, Tisserand parameter with respect to Jupiter $T_J > 3.05$, and semimajor axis $a < 30.1$ au (as well as implicitly an eccentricity $e < 0.756$). Due to the lack of community consensus on Centaur orbital definition, we also explore two alternative definitions for Centaurs to investigate the effects that differing population coverage in orbital space has on overall detections. We look at the definition set out in G. Sarid et al. (2019, hereafter referred to as the S19 sample), namely $q > 5.2$ au and aphelion distance $Q < 30.1$ au (and $e < 0.71$) —a definition that places objects entirely within the giant-planet region, giving insight into the transition objects not accounted for within the G08 sample, but excluding eccentric objects with aphelia more distant than Neptune's orbit. Finally, we also employ a hybrid definition (hereafter referred to as the Hybrid sample), with $q > 5.2$ au and $a < 30.1$ au (and $e < 0.83$) and no aphelia constraints—this has the benefit of including the base giant-planet-crossing orbits that make up the bulk of the known Centaurs, while also including those on more eccentric and hence distant perihelia orbits, as well as those near transition objects included in the S19 sample.

The resulting orbital distributions for all three models are shown in Figure 2. The G08 and Hybrid models appear the most similar owing to the Hybrid otherwise containing only ∼150,000 low-q objects that do not appear in the G08 model. Conversely, the S19 model does not contain as many high semimajor axis objects, with a median value of ∼21 au. All three broadly share the same eccentricity and inclination distributions, with the majority being concentrated in a central $e = 0.1$–$0.5/i = 0°$–$50°$ range—approximately 1% of each model is, however, also composed of retrograde ($i > 90°$) orbits. All three definitions of these models are summarized in Table 1. The following sections detail how we developed the G08 model for the Centaurs, with Section 2.4 looking at the differences in this process needed to construct the two alternative models.

2.3.1. Orbital Distribution

We model the underlying Centaur population based on the end results of the N-body integration from D. Nesvorný et al. (2019). Here a planetesimal disk of 10^6 particles (including 4000 Pluto-sized objects below 30 au) was integrated with a grainy Neptune migration—here Neptune starts at a semimajor axis of 24 au and is simulated to present day with exponential e-folding timescales of $\tau_1 = 30$ Myr and $\tau_2 = 100$ Myr representing its migration at two stages, respectively. During the final Gyr of simulation, if an individual particle orbit reached a semimajor axis $a < 30$ au, it was cloned 100 times via random small changes to their velocity vectors ($\delta V/V \sim 10^{-5}$) and

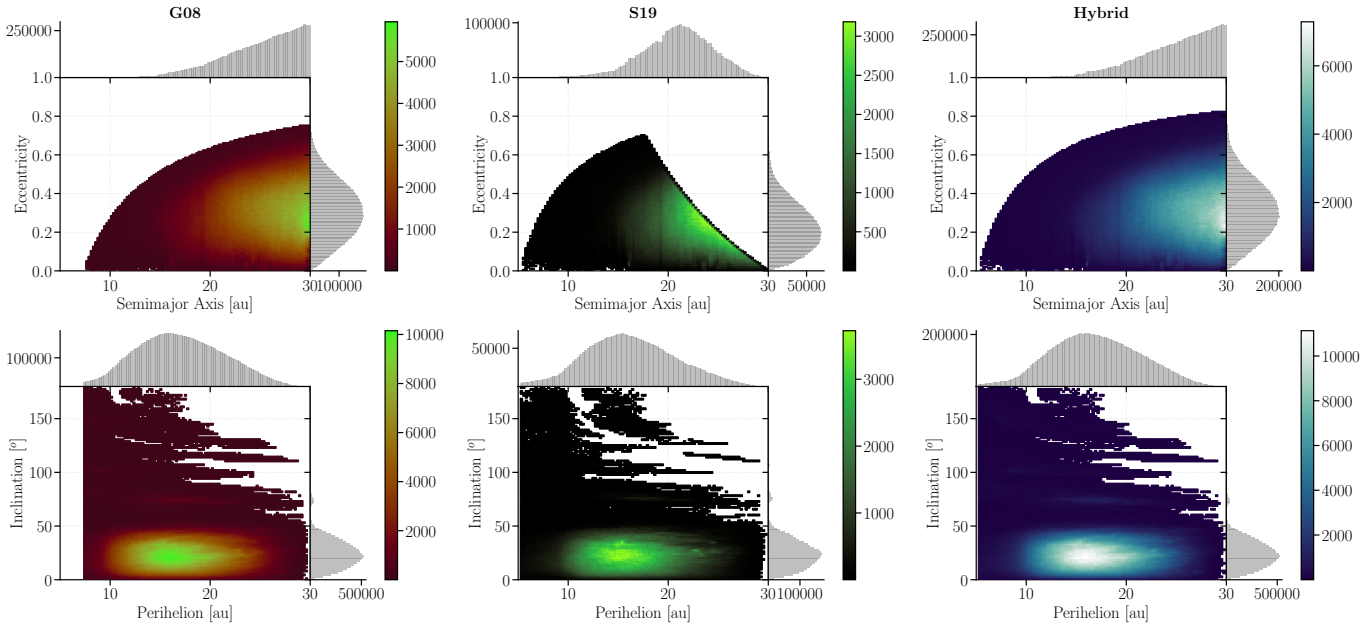

Figure 2. Orbital space 2D histograms for the three dynamical classifications of the input Centaur models used in this work, namely the G08 sample in the left column, the S19 sample in the middle column, and the Hybrid sample in the right column. The top row shows histograms of Centaur eccentricity as a function of semimajor axis, whereas the bottom row shows histograms of Centaur inclination as a function of perihelion distance.

Table 1
Dynamical Definitions for Each Orbital Distribution

	q (au)	a (au)	Q (au)	e
G08 sample	>7.35	<30.1	⋯	<0.756
S19 sample	>5.2	⋯	<30.1	<0.71
Hybrid sample	>5.2	<30.1	⋯	<0.83

saved with a 10^4 yr cadence. After removing cometary and Trojan orbits and applying the G08 dynamical definition, this steady-state Centaur population of $\sim 2.6 \times 10^7$ objects was then biased using the OSSOS survey simulator (S. M. Lawler et al. 2018a) and found to be consistent with actual OSSOS Centaur discoveries at the 1σ level. Orbital distributions are randomly drawn from this output in *a, e,* and *i* together, allowing for more than one object to have the same $a/e/i$ combination. As the output angular elements are uncorrelated with each other, and in order to avoid clustering of the orbits, the angular elements ω, Ω, and M are each randomly sampled from a continuous uniform distribution $U \in [0°, 360°)$ to account for the effects of orbital precession due to interactions with the giant planets from the original (D. Nesvorný et al. 2019) simulation orbits. The resulting input orbital distribution of the G08 model is highlighted in Figure 2.

2.3.2. Absolute Magnitude Distribution

The physical size and albedo of an object will affect its brightness and hence how observable it will be. Including a physical size distribution in our model requires assumptions of albedo and color distributions that remain correlated (A. Alvarez-Candal et al. 2016, 2019; C. Ayala-Loera et al. 2018) and are poorly constrained for the Centaur population with current samples. Instead, we opt to use a more easily modeled H_r distribution, as it is related directly to the measured apparent magnitude. The apparent magnitude m (ignoring rotational effects or activity—we assume that our population is entirely inactive; see Section 3.3 for further discussion on the effects of activity) of an object at a given heliocentric distance r, geocentric distance Δ, and phase angle between Sun–object–observer α (whose effect on the scattering geometry is modeled by the phase function Φ) is defined as

$$m(\alpha, r, \Delta) = H + 5\log_{10}(r\Delta) + \Phi(H, \alpha). \quad (2)$$

The size distribution of TNOs displays a "break" or a "knee" at diameters $D \sim 100$ km, or an absolute magnitude $H_r = 7.7$ (C. Shankman et al. 2013; W. C. Fraser et al. 2014; S. M. Lawler et al. 2018b). As such, they are modeled with a two-part power-law distribution, with different slope values being observed on either side of the break. As with D. Nesvorný et al. (2019), however, we opt to model the absolute magnitude distribution as a single power law as defined by the following cumulative distribution:

$$N(\leqslant H_r) = N_0 10^{\alpha_0 (H_r - H_0)}, \quad (3)$$

where the slope parameter $\alpha_0 = 0.42$, as per OSSOS observations (C. Shankman et al. 2016; S. M. Lawler et al. 2018b). The value N_0 is a scaling factor representing the cumulative number of objects with an absolute magnitude $H_r \leqslant H_0$. This yields $\sim$33 objects with $H < 7$, compared to roughly 20 objects from the knee power law in S. M. Lawler et al. (2018b). The difference of around 13 objects is less than 1% of our final discovery results in Section 3.1 and smaller than the random variation between runs.

We adopt scaling constants of $N_0 = 21{,}400$ and $H_0 = 13.7$ for our G08 sample of Centaurs, in line with recent estimates for the intrinsic G08 definition of Centaurs from the debiased Pan-STARRS search of J. A. Kurlander et al. (2025). We note that, within their stated population uncertainty of $^{+3400}_{-2800}$, this result is also consistent with the original debiased OSSOS population estimate of $21{,}000 \pm 8000$ Centaurs with $H_r < 13.7$ from D. Nesvorný et al. (2019). We opt for the

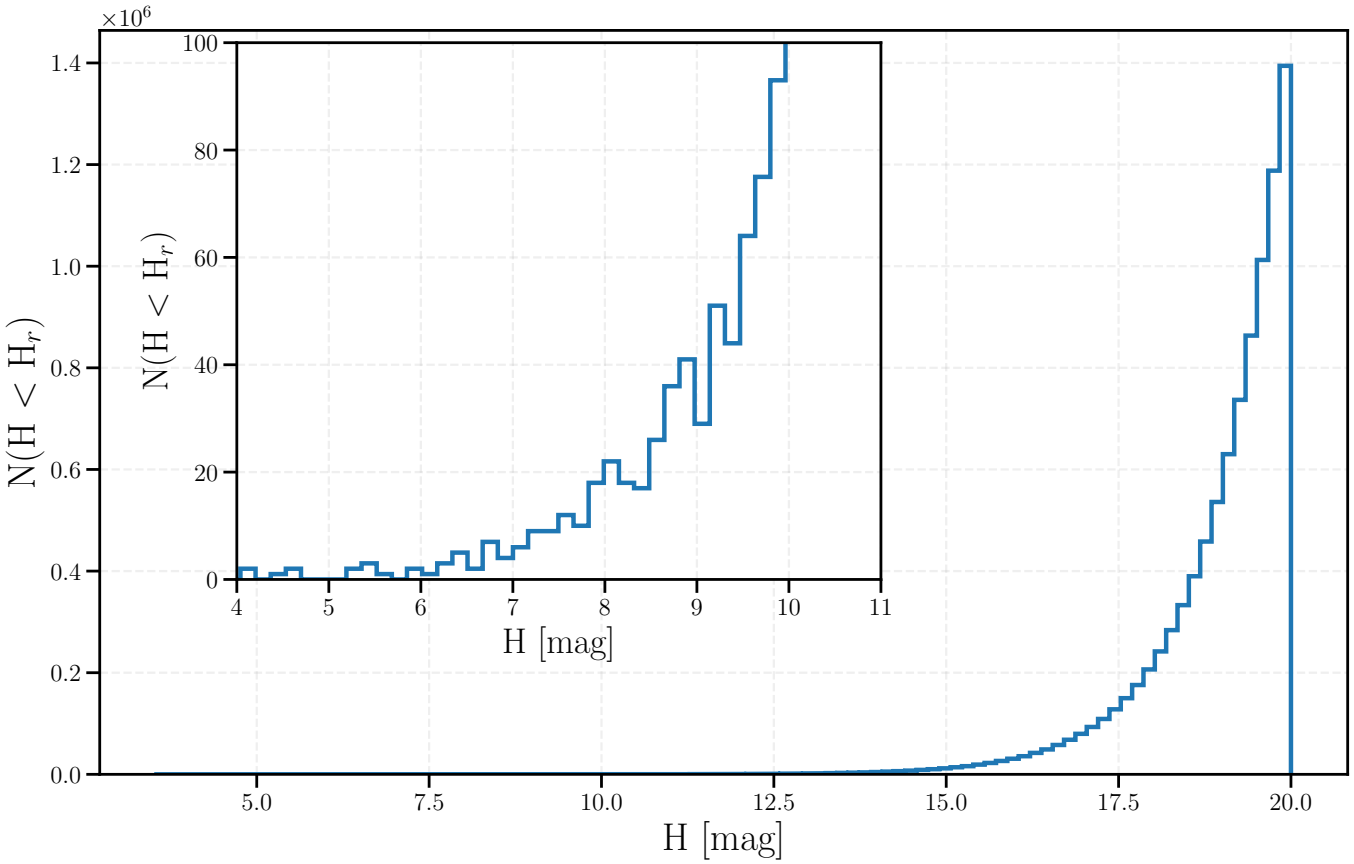

Figure 3. Cumulative histogram of the model absolute magnitude H distribution of objects with H less than a given absolute magnitude H_r for the G08 sample. The inset represents a zoom-in of the bright end of the same distribution where $H < 11$.

J. A. Kurlander et al. (2025) value over the D. Nesvorný et al. (2019) estimate, however, due to it being a more well-constrained estimate. Each object to be simulated must be assigned an absolute magnitude from the distribution in Equation (3). In order to find the maximum H_r value that we need to simulate in our synthetic population, we first take the faintest 5σ depth across all six *ugrizy* bands recorded in the baseline cadence simulation ($\sim$26.2). Assuming that an object is on a circular orbit with a perihelion distance of $\sim$5.2 au (with no phase effects), we then calculate an absolute magnitude using Equation (2). From this, the faintest detectable object would have an $H_r \sim 19$; however, the LSST limiting magnitude represents a detection efficiency of 50% (see Section 2.1, Equation (1)). Objects that are slightly fainter will therefore still have a chance of being detected. As such, assuming a detection efficiency function as detailed in S. R. Merritt et al. (2025), we increase this value by a magnitude to $H_r = 20$ in order to account for this effect. Combined with the previously discussed scaling factors of α and N_0, we find that we need to simulate $N(H_r < 20) \sim 9.47 \times 10^6$ Centaurs. We then uniformly sample $N(H_r < 20)$ number of orbits from our orbital model and assign them H values via an inverse transform of Equation (3), given by Equation (4) and highlighted in Figure 3:

$$H_r = \frac{1}{\alpha} \log_{10}\left(\frac{N(<H_r)}{N_0}\right) + H_0. \quad (4)$$

(2060) Chiron is the largest Centaur ($H_V = 5.59$) reported in the MPC to date. Our H distribution produces eight objects larger than (2060) Chiron, of which three are brighter than apparent magnitudes of $m_r = 21.5$ and one lies within $\pm 10°$ of the ecliptic upon applying our orbital model. This is consistent with the observational constraints of Centaur discoveries from the Pan-STARRS Centaur survey in J. A. Kurlander et al. (2025), who did not discover any new bright objects. It is also roughly consistent with previous shallow surveys that have contributed to the bulk of the MPC Centaur discovery catalog.

2.3.3. Colors

The LSST will observe across six different filters; therefore, we must account for the surface colors of Centaurs within our model population. Centaurs have been shown to display a bimodality in their color distribution, similar to that of the larger TNO population (S. C. Tegler & W. Romanishin 1998, 2000, 2003; N. Peixinho et al. 2003; M. A. Barucci et al. 2005; D. Perna et al. 2010; I. Wong & M. E. Brown 2017), due in part to their shared dynamical history with the small hot TNO populations (M. J. Duncan & H. F. Levison 1997; H. F. Levison & M. J. Duncan 1997; K. Volk & R. Malhotra 2008; W. C. Fraser & M. E. Brown 2012; N. Peixinho et al. 2012). We use optical spectra of two canonical Centaurs as model objects: the "red" Centaur (5145) Pholus from S. Fornasier et al. (2009), D. Perna et al. (2010), and M. A. Barucci et al. (2011), and the "blue" Centaur (54598) Bienor from A. Alvarez-Candal et al. (2008), A. Guilbert et al. (2009), and D. Perna et al. (2010). As Centaur and (small-sized) TNO spectra remain mostly featureless in the optical spectrum (A. Alvarez-Candal

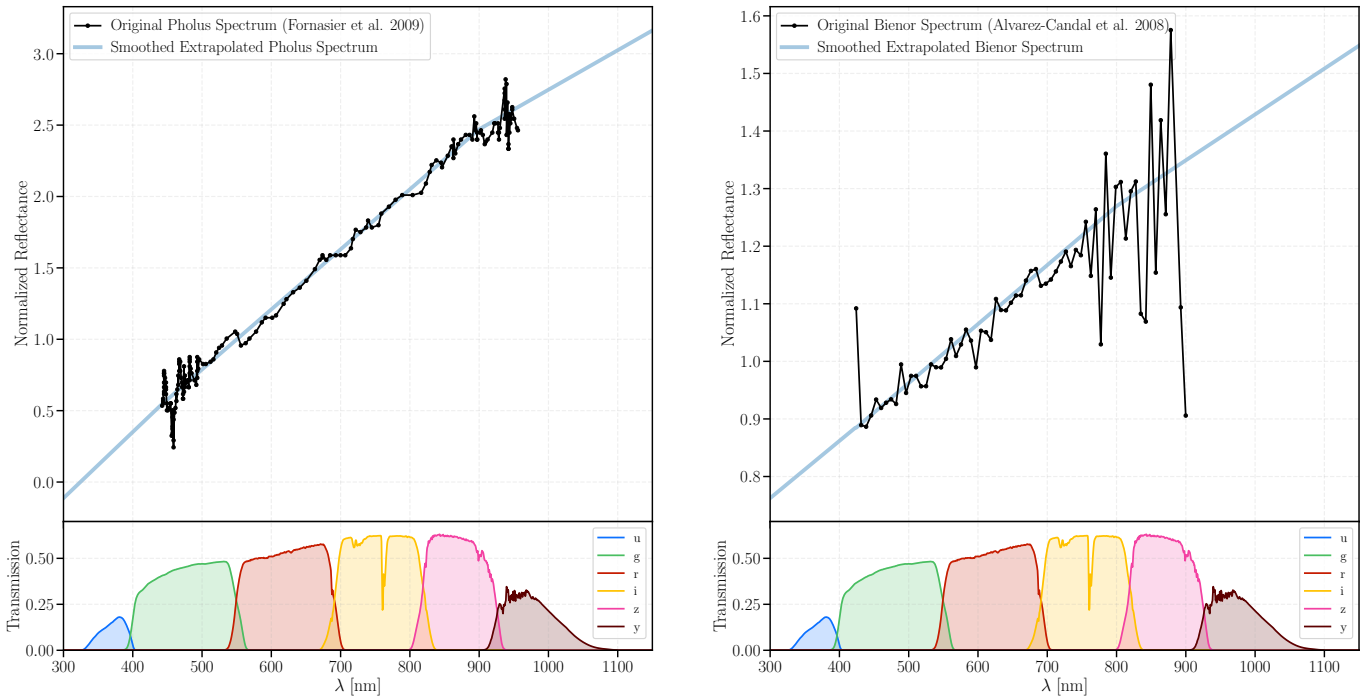

Figure 4. Original reflectance spectra of Pholus (left; S. Fornasier et al. 2009) and Bienor (right; A. Alvarez-Candal et al. 2008), normalized at 550nm. Overlaid are the new extrapolated, smoothed "spectra" that are used to convert to SEDs and obtain color estimates. Below are the LSST filter throughputs for wavelength range reference. Note that Bienor's spectrum has been smoothed starting at ∼750 nm in order to account for the increased noise in the proceeding range.

et al. 2008; K. M. Barkume et al. 2008; M. A. Barucci et al. 2008, 2011; S. Fornasier et al. 2009; M. E. Brown 2012; M. A. Barucci & F. Merlin 2020), we use the `curve_fit` function from `scipy` (P. Virtanen et al. 2020) to determine slopes at both red and blue ends of the existing spectra, extending and smoothing over the noise at both ends to LSST filter wavelength ranges. In order to account for noise in the original spectra, we also smooth over the original data by applying a linear fit. The resulting three-component spectra are shown in Figure 4. We multiply by the solar spectrum (R. L. Kurucz 2005) again to convert these spectra to spectral energy distributions (SEDs), and then we integrate the resulting flux under the LSST filter bandpasses via `phot_utils` functions within `rubin_sim`. The resulting colors are given in Table 2. We then use the blue:red color fraction of 3:1 as determined by I. Wong & M. E. Brown (2017), giving 75% of our model population a Bienor-like color and 25% a Pholus-like color. This is, however, a first approximation for the population —in Section 3.1 we discuss the impact that our choice of color distribution has on discoverability.

Table 2
Estimated LSST Colors of Bienor and Pholus

LSST Color	Pholus (Red) Colors (mag)	Bienor (Blue) Colors (mag)
$u-r$	3.45	1.86
$g-r$	1.00	0.56
$i-r$	−0.50	−0.23
$z-r$	−0.73	−0.33
$y-r$	−0.89	−0.41

2.3.4. Phase Curves

In order to accurately calculate the apparent magnitude of each Centaur, phase effects must be accounted for. As a Centaur moves very little in its orbit during the LSST survey, the change in viewing geometry illuminating different surface fractions will not contribute considerably to their brightness changes; instead, Centaur brightness variations are driven by the backscattering of light from surface particles (D. L. Rabinowitz et al. 2007). For Centaurs, this change in brightness tends to be linear (M. W. Buie et al. 1992; P. Rousselot et al. 2005; S. Bagnulo et al. 2006; D. L. Rabinowitz et al. 2007; I. N. Belskaya et al. 2008; B. E. Schaefer et al. 2009; A. J. Verbiscer et al. 2013; S. Fornasier et al. 2014; C. Ayala-Loera et al. 2018; M. M. Dobson et al. 2023), with a slope measurable as β using the following equation for the reduced magnitude (the apparent magnitude scaled to a geocentric and heliocentric distance of 1 au):

$$M(\alpha) = H + \alpha\beta, \tag{5}$$

where H is the absolute magnitude and α is the phase angle of the Sun−object−observer.

We apply a phase function to each Centaur by assigning each synthetic body a linear phase coefficient of $\beta = 0.071$ mag deg^{-1}—this is derived from the mean of the ensemble sample of 23 Centaurs and their measured linear phase coefficient from C. Ayala-Loera et al. (2018), A. Alvarez-Candal et al. (2016), and D. L. Rabinowitz et al. (2007). The value of β is itself a function of the photometric filter being observed in; however, due to the small sample size of measured Centaur phase coefficients, we uniformly assign this across all filters.

2.4. Alternative Centaur Models

With the G08 model now fully defined in terms of orbital distribution, absolute magnitude distribution, surface colors, and phase behavior, we next explore constructing S19 and

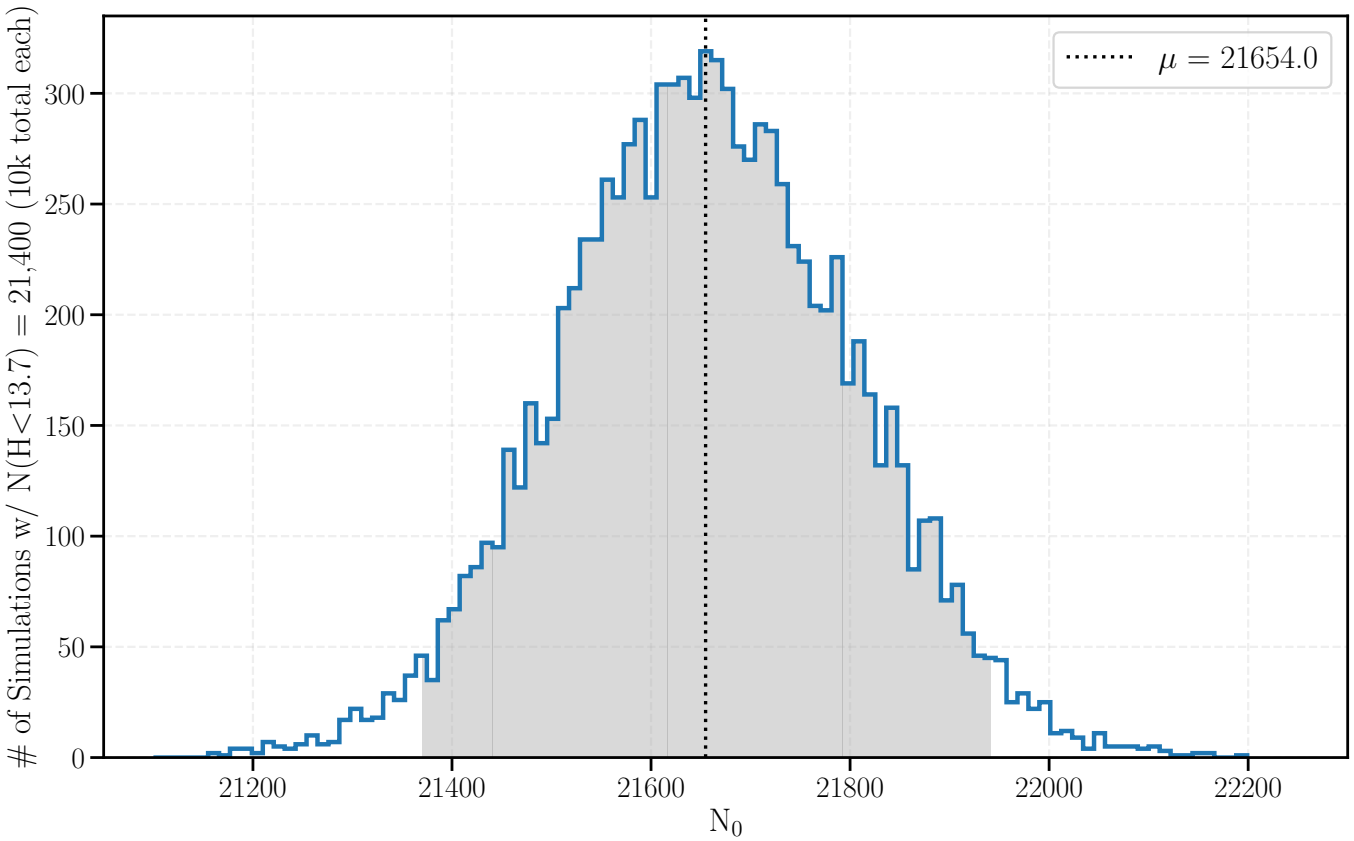

Figure 5. Histogram showing the number of 10,000 simulations of each trial N_0 value for the Hybrid definition that match the G08 sample scaling of $N(H < 13.7) = 21{,}400$. The dashed line represents the mean value of the distribution, and the shaded region is the 95% confidence interval.

Hybrid definition Centaur models to investigate how different Centaur orbital space classifications affect discovery predictions. The scaling parameter N_0 for the absolute magnitude distribution, which effectively controls the number of objects to be simulated, was calibrated to Pan-STARRS (in the case of J. A. Kurlander et al. 2025) or OSSOS (in the case of D. Nesvorný et al. 2019) detections of Centaurs that matched the G08 definition and as such cannot be applied to the S19 or Hybrid models. Definitionally, however, the G08 orbital space overlaps entirely with that of the Hybrid model. The Hybrid sample may also be calibrated to OSSOS observations therefore by selecting the subset of orbits within the Hybrid model that match the G08 definition. The scaling parameter N_0 can then be tuned for these selected orbits until the same value of $N(<13.6) = 21{,}400$ is obtained. We trial a grid of N_0 values around the initial value of $N_0 = 21{,}400$, from 21,100 to 22,200—for each value of N_0, Hybrid orbits are sampled from the original D. Nesvorný et al. (2019) model (as described in Section 2.3.2) and the G08 orbits within selected. The cumulative count $N(< 13.7)$ is then checked for this selected distribution against the G08 value of 21,400—this is repeated 10^5 times for each N_0, with a tally kept for each time the $N(<13.7)$ values match. The resulting distribution of matched $N(<13.7)$ values is shown in Figure 5—from this the median value of $N_0 = 21{,}654$ is selected and used in Equation (3) for the Hybrid sample, resulting in $N(H_r < 20) \sim 9.58 \times 10^6$ Centaurs to be simulated. As the Hybrid sample is now absolutely calibrated to OSSOS/Pan-STARRS-detected Centaurs, similarly the S19 orbits that overlap within the Hybrid orbits are selected in order to obtain the calibrated S19 sample of $N(H_r < 20) \sim 3.13 \times 10^6$ Centaurs. The process for obtaining colors and phase-curve slopes for both new models are the same as outlined for the G08 sample.

3. Results

Throughout the following section, we present the results for the simulated G08, S19, and Hybrid Centaurs through `Sorcha` that pass the linking criteria outlined in Section 2.1. All results utilize the one snap version of the LSST cadence simulation—the overall on-sky time is comparable between one-snap and two-snap simulations, only the distribution of when visits occur changes. As such, the following results remain consistent for both versions of the simulations.

3.1. Discovery Yield

Figure 6 shows the number of unique Centaur discoveries for each definition over the 10 yr survey lifetime. We find the total number of Centaurs discovered over the decade to be 1524, 1170, and 1967 for the G08, S19, and Hybrid definitions, respectively—the total discoveries after years 1, 2, 5, and 10 are highlighted in Table 3, and the orbital space that the discovered Centaurs cover is shown in Figure 7. These values are based on an assumed color fraction described in Section 2.3.3; however, we have additionally varied this fraction from two extremes of 90:10 to 10:90 blue:red. This has little effect on the yield, however, only changing the final number of discovered Centaurs on the order of $\lesssim 10^1$, and so for the rest of this paper we continue analysis using our initial assumption of a 3:1 ratio. The results presented here are the product of one instance of a model simulation, with nondeterministic results due to randomly assigned absolute magnitudes and surface colors, as

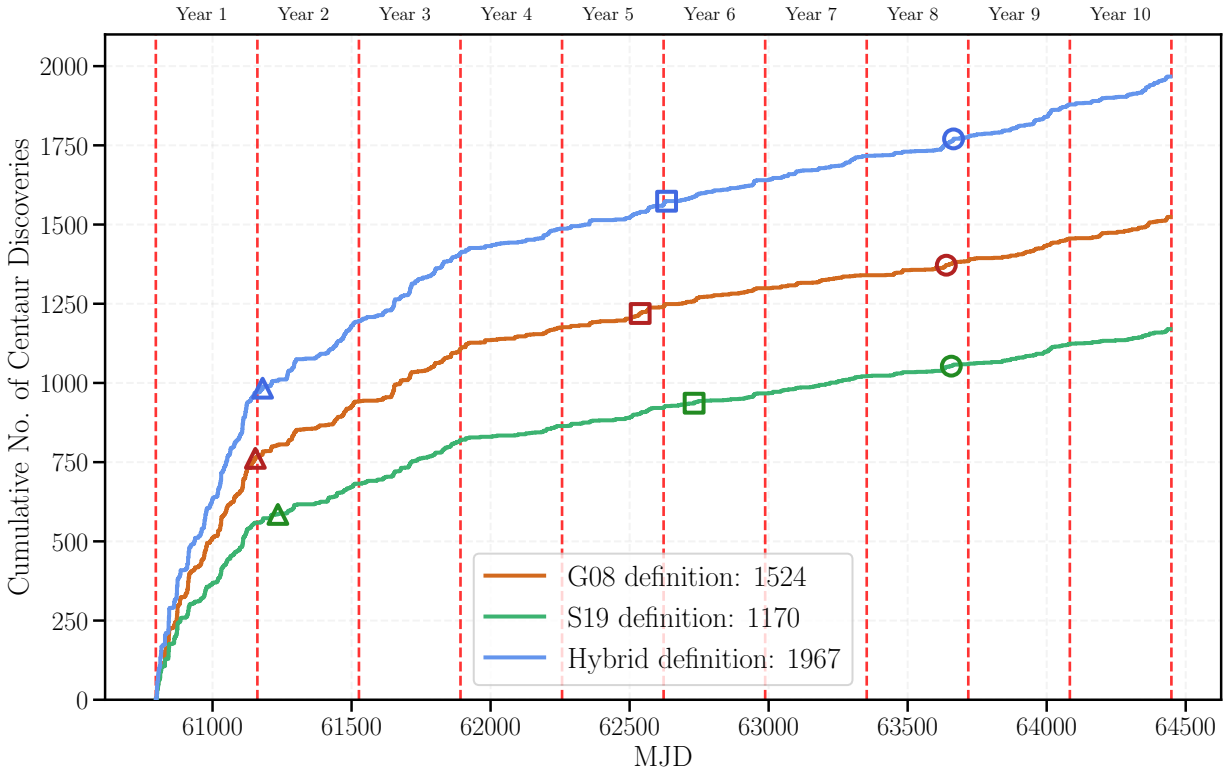

Figure 6. Cumulative histogram (with a bin size of 1 day) of the discovery rates of the different Centaur definitions over the 10 yr LSST lifetime. Red dashed lines demark yearly boundaries for the survey, with labels above each block to highlight the year of operation. We highlight the points of 50% (open triangle), 80% (open square), and 90% (open circle) completion for each population.

Table 3
Numbers of Centaur Discoveries by Survey Year for Each Dynamical Definition, Compared to the Number of Known Centaurs within the MPC for Each Corresponding Definition

	LSST Discovery Numbers				MPC
	1 yr	2 yr	5 yr	10 yr	Population
G08 sample	767	942	1240	1524	215
S19 sample	559	682	922	1170	186
Hybrid sample	970	1195	1563	1967	288

well as randomization within `Sorcha` applying survey biases. The uncertainty on 100 simulations of unique models for each definition is ∼5%–8%.

Centaur discovery is seen to be rapid, with 50% of each population discovered shortly after the beginning of the second year of the LSST's operation. Among all definitions, year 1's discovery rate stands out compared to all following years. The median r-band apparent magnitude of discovered objects decreases from ∼22.7 in year 1 to ∼23.5 across the remainder of the survey—the vast majority of bright objects are discovered within the first year, with the discovery rate in following years being dominated by the LSST limiting magnitude (∼24.7 for r; Ž. Ivezić et al. 2019; F. B. Bianco et al. 2022). Fainter objects are continuously detected as they gain more observations and so more chances at being detected and passing the SSP linking pipeline. Across all three definitions, ⩾96% are discovered with an ecliptic latitude $-40^\circ \leqslant b \leqslant 40^\circ$ as shown in Figure 8; however, outside of this, between the three models, ∼3–14 objects are discovered with ecliptic latitude $\leqslant -70^\circ$. As most Centaur discoveries have so far been located closer to the ecliptic plane, an increased sample size of high ecliptic latitude Centaurs will offer a unique probe into a more dynamically stable Centaur population, as these objects experience less frequent close encounters with giant planets.

The LSST will discover ∼7–12× more faint objects than are known today, with ∼80 Centaurs with $H \geqslant 12$ recorded in the MPC compared to ∼600–950 in all three of our samples. The distributions in the absolute magnitude and median apparent magnitudes of detected Centaurs are shown in Figure 9. Table 3 also includes a reference to the known MPC numbers for each respective population. Comparing to the 215, 186, and 288 definitions of G08, S19, and Hybrid, respectively, this shows a ∼6-to-7-fold increase in sample size. As a comparison, out of the previous well-characterized solar system discovery surveys, the Dark Energy Survey discovered a single Centaur (limiting magnitude in r band, $m_{\mathrm{lim},r} \sim$ 24.0; P. H. Bernardinelli et al. 2022), OSSOS discovered 20 ($m_{\mathrm{lim},r} \sim$ 24.1–25.2; M. T. Bannister et al. 2018; N. Cabral et al. 2019), Pan-STARRS1 discovered 78 (unknown) ($m_{\mathrm{lim},V} \sim$ 22.5; R. J. Weryk et al. 2016), and the Deep Ecliptic Survey found 13 ($m_{\mathrm{lim},r} \sim$ 26.2; J. L. Elliot et al. 2005). These surveys' primary science goals were not, however, focused on Centaur discovery—they had differing sky coverage, depths, fields of view, and relative coverage of Centaur orbital space, and their results must therefore be interpreted with appropriate caveats.

With an increased data set of Centaurs across a wide orbital space range, the LSST will be able to provide insights into the dynamical transition from Centaur toward JFC. G. Sarid et al. (2019) posited that existence in the JFC population is preceded by residence in a dynamically short-lived corridor of orbital space known as the "Gateway" region (5.2 au $< a <$ 7.8 au, $e < 0.2$). This region also coincides with observed heliocentric

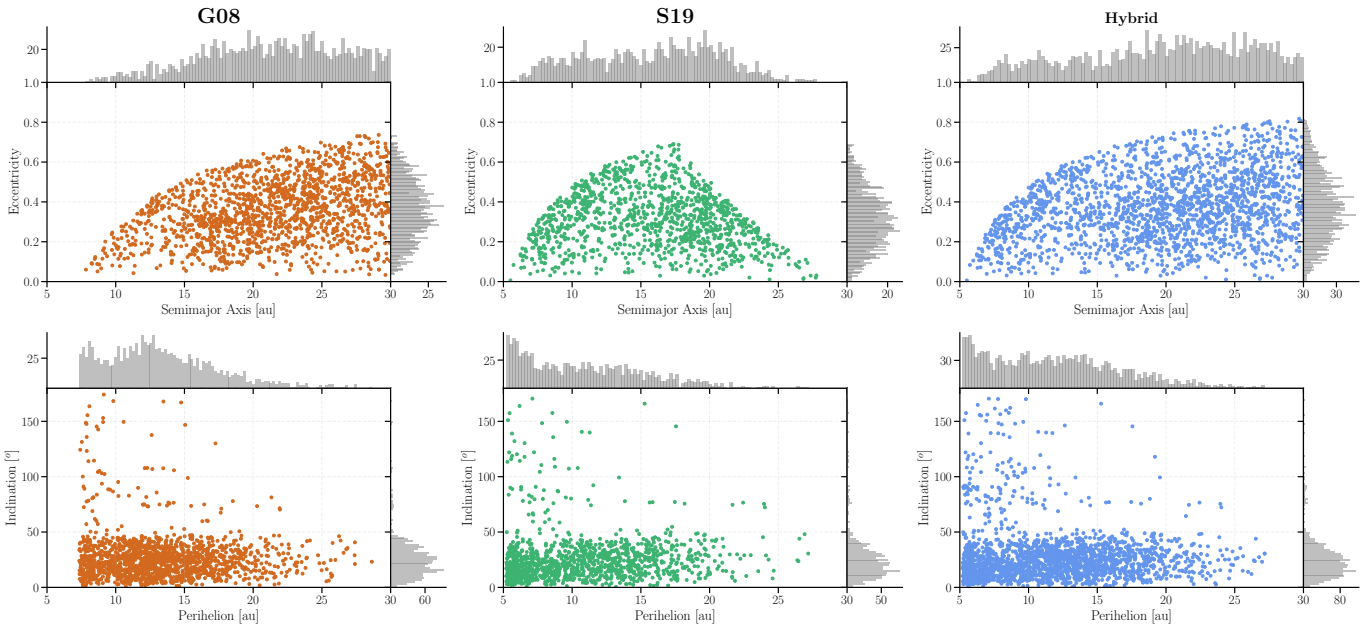

Figure 7. Scatter plots of the orbital spaces covered by discovered objects, similar to Figure 2. Once again the columns represent the three respective definitions, whereas the top row represents Centaur eccentricity as a function of semimajor axis, and the bottom row represents Centaur inclination as a function of perihelion distance.

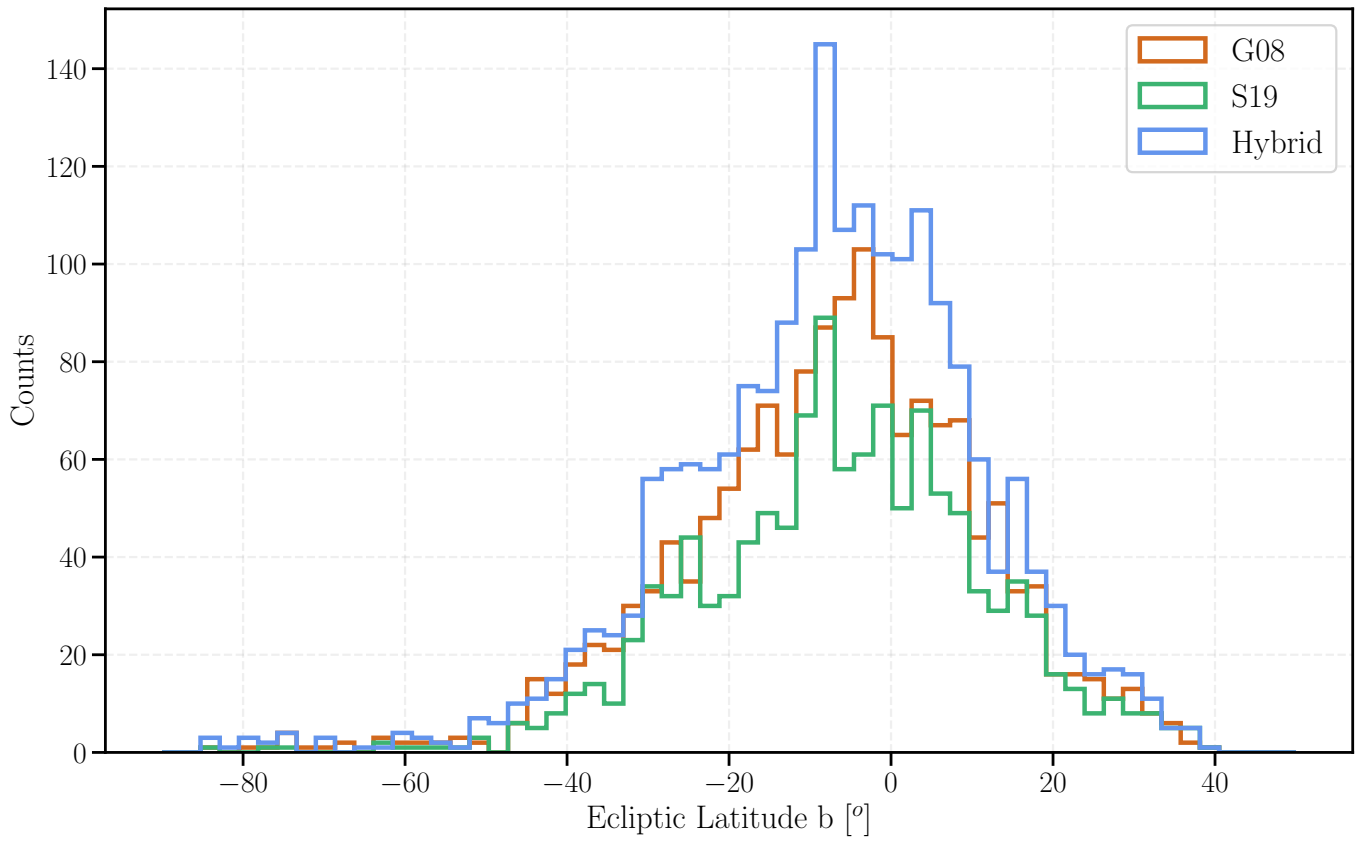

Figure 8. Histograms of the ecliptic latitudes for each of the G08 (red), S19 (green), and Hybrid (blue) definitions at the time of each object's discovery.

distances that show increases in cometary activity of Centaurs (W. C. Fraser et al. 2022; A. Guilbert-Lepoutre et al. 2023). More recent thermal and dynamical modeling from A. Guilbert-Lepoutre et al. (2023) has, however, contrasted with this result, showing that only ∼20% of Centaurs are dynamically new to the Gateway prior to becoming JFCs, with several transitions between the two populations frequently occurring and the majority (∼80%) transitioning outside of the Gateway altogether. Regardless of the dynamical pathway to becoming a JFC, study of objects within this Gateway region offers unique probes into statistically higher processed surfaces of Centaur. Within the S19 sample (and S19 group within the Hybrid

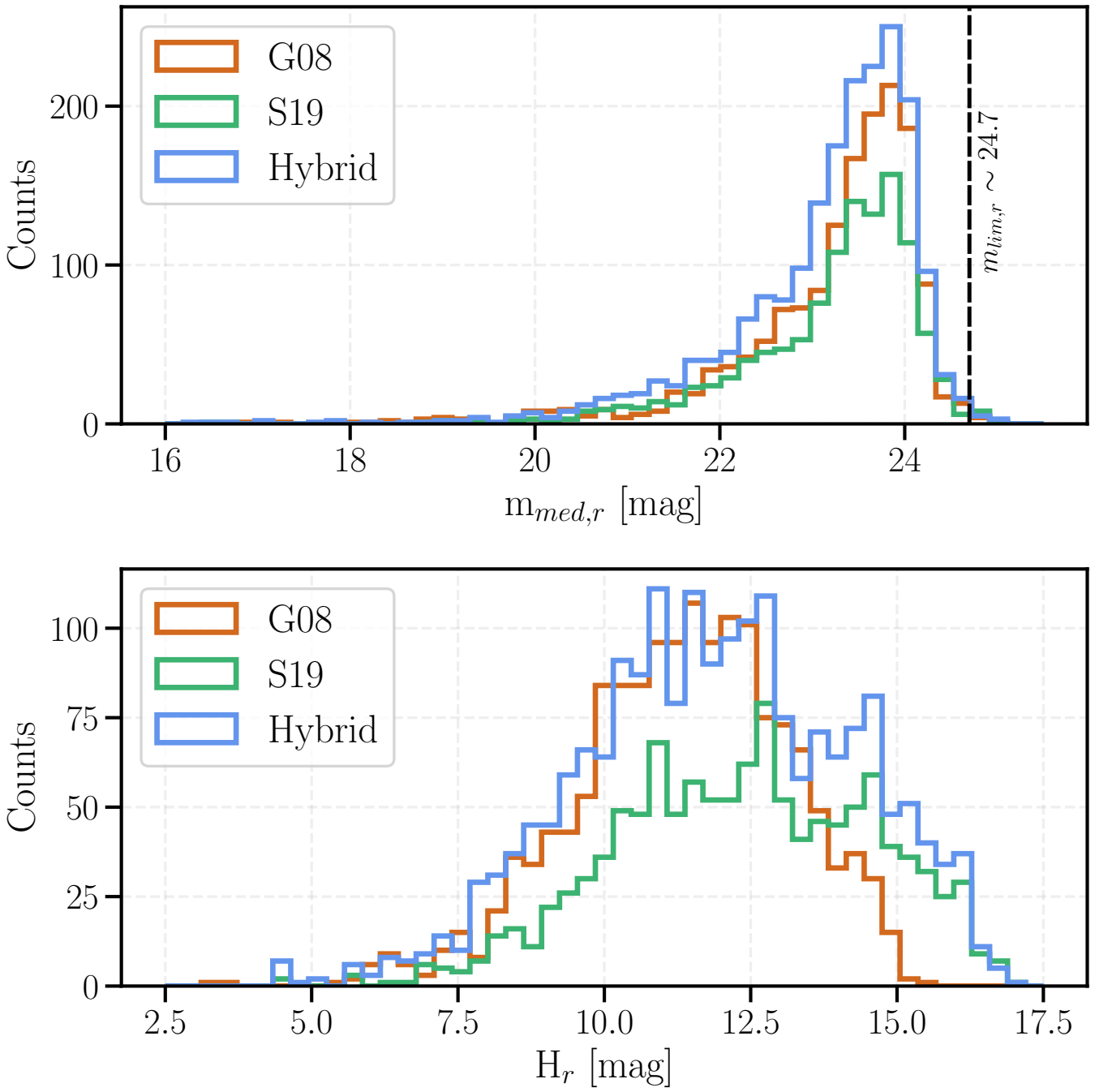

Figure 9. Histogram on top of the median apparent magnitude of discovered Centaurs in the *r* band, separated by G08, S19, and Hybrid definitions, overplotted with a dashed line of the limiting magnitude in the LSST *r*. Below is a histogram of the same sample's absolute *r*-band magnitudes.

sample), we find ∼10–15 objects within the Gateway region—a ∼3-to-5-fold increase in the number of Gateway Centaurs in previous studies (I. Kulyk et al. 2016; G. Sarid et al. 2019; J. K. Steckloff et al. 2020; H. H. Hsieh et al. 2021; T. Kareta et al. 2021; D. Z. Seligman et al. 2021; A. Guilbert-Lepoutre et al. 2023). Studies of their surface properties through color analysis (see Section 3.4) will thus be a means to shed light on the dynamical origins and present-day states of these Centaurs.

3.2. Observation Numbers

Over the full 10 yr, detected Centaurs will receive a large number of observations, with a median of 220, 200, and 207 for the G08, S19, and Hybrid definitions, respectively (assuming perfect performance of association and precovery from the SSP; M. Jurić et al. 2020)—these are further broken down per filter in Figure 10 and Table 4. The LSST will also continuously observe ∼60%–70% of the discovered objects (or 1046, 677, and 1181 discovered G08, S19, and Hybrid Centaurs, respectively), as they are observed for nearly the full 10 yr duration of the survey. Per year, this equates to a median of ∼24 observations across all filters for all three samples. Observations before linking may only become identified by the SSP pipelines as the orbit is refined. In all three samples we find that ⩾99% of discovered Centaurs will achieve orbital arcs longer than a year, which will typically enable good orbit determination (see K. Volk & C. Van Laerhoven 2024).

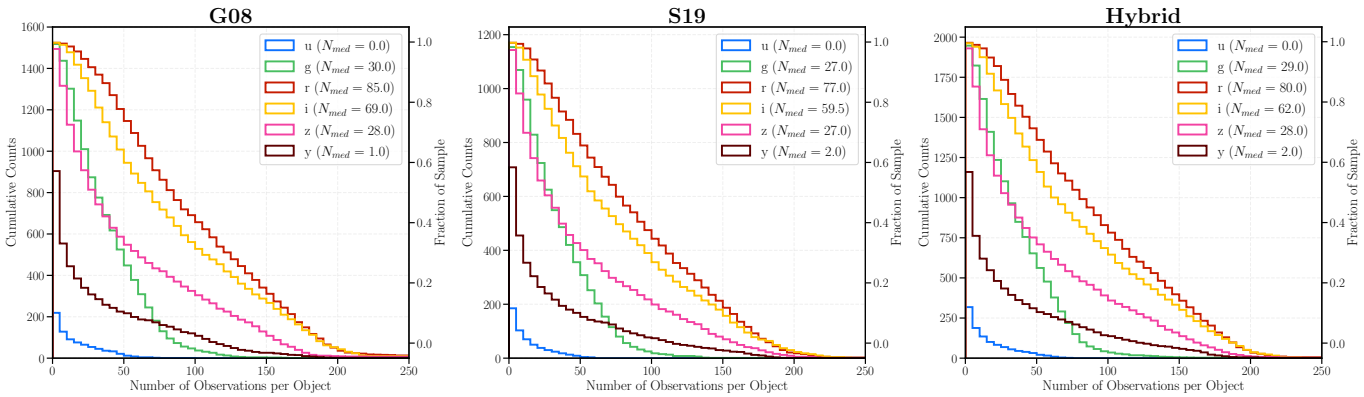

Figure 10. Cumulative histograms of the number of observations each object detected in each sample will obtain, broken down by filter—excluding those observations that fall within the COSMOS DDF. Note that for all of these plots the *x*-axis is cut off at 250 for readability; however, the G08 sample extends to ∼800, the S19 sample extends to ∼650, and the Hybrid sample extends to ∼900 owing to objects entering DDFs. The reported median values in the legends include these values.

Table 4
Breakdown of the Median Number of Observations per Object (Including Zero Observations) over the Full LSST Survey Lifetime, as Split into Each Filter for Each Centaur Definition—Excluding Observations That Fall within the COSMOS DDF

Sample	Median No. of Observations per Object						
	u	*g*	*r*	*i*	*z*	*y*	All Filters
G08	0	31	86	69	28	1	220
S19	0	28	78	61	27	2	200
Hybrid	0	29	82	63	29	2	207

Note. Also shown in the rightmost column is the median number of observations per object across all filters. All columns assume perfect association and precovery from the SSP.

Different footprints of the LSST will have different numbers of visits, with DDFs being single fields with a much larger sampling rate than the surrounding WFD area. The number of observations is enhanced for those Centaurs that fall within the DDFs—in particular the COSMOS DDF (centered at $10^{h}00^{m}24^{s}/+02^{d}10^{m}55^{s}$), which at ∼9° latitude off of the ecliptic makes it particularly sensitive to mildly dynamically excited populations such as the Centaurs. Examining our simulation outputs, only 30, 35, and 46 Centaurs in the G08, S19, and Hybrid samples (or ∼5% of each definition's total discoveries) are ever in the COSMOS DDF throughout the 10 yr survey. Centaurs will not spend more than one observing season within the 3.°5-diameter COSMOS DDF—regardless, this is enough time to boost observations to the order of thousands. COSMOS DDF Centaurs receive on average ∼400–500 observations, with the median time spent in the COSMOS DDF being typically ∼100 days (however, some approach 500 days, and one reaches ∼4 yr). In comparison, a Centaur that resides solely in other regions of the survey footprint will achieve half the number of observations over 10 yr. With the sheer number of observations, those few objects that do pass within the COSMOS DDF will make interesting candidates for light-curve and cometary activity analysis.

3.3. Cometary Activity

Centaur activity, unlike that of JFCs, is not solely linked to perihelion distance (although most known active Centaurs have a $q < 12$ au; see E. Lilly et al. 2024) and has been seen to be possible at any stage of their orbits (N. Peixinho et al. 2020). It is thought to be driven by as-of-yet-unknown mechanisms rather than the water-ice sublimation of JFCs (see D. Prialnik 1992; D. Jewitt 2009; N. Peixinho et al. 2020, and references therein). The LSST detection estimates outlined in Sections 3.1 and 3.2, which are based on an inactive Centaur population, thus represent only a lower limit, as activity can cause increases in brightness on the order of ∼1–5 mag (T. Kareta et al. 2020; J. K. Steckloff et al. 2020; H. H. Hsieh et al. 2021; M. M. Dobson et al. 2024). This in turn will allow for smaller active objects to be observable within our samples, particularly in the innermost regions of Centaur orbits, where activity is mostly observed. Estimates from D. Jewitt (2009), N. Peixinho et al. (2020), and C. O. Chandler et al. (2024) all place the activity occurrence rate for Centaurs at ∼9%–13%, which represents in our samples ∼100–250 active Centaurs observed.

Recent work by E. Lilly et al. (2024) has shown evidence of jumps in semimajor axis over months to years being a precursor to the onset of such cometary activity, with the need for monitoring to probe this potential trend. E. Mazzotta Epifani et al. (2018) also discuss the need for the monitoring of already active Centaurs and their surface colors as a means of following the evolution of the previously discussed bimodal color distribution. With observational arcs approaching a decade for hundreds of Centaurs, the LSST is able to provide just such a monitoring service for these objects. With ∼700–1100 discovered Centaurs each gaining ∼24 observations a year, activity searches will be possible in the form of probing extensions of the PSF of each object or direct coma detection (e.g., D. Jewitt 2009; E. Mazzotta Epifani et al. 2018; T. Seccull et al. 2019; M. M. Dobson et al. 2024). Alongside this, deviations in the phase curves of each object will also be usable as a means to search for activity (e.g., M. M. Dobson et al. 2023, 2024)—see Section 3.4 for further discussion on the predictions for Centaur phase-curve measurements within the LSST.

3.4. Colors, Light Curves, and Phase Curves

Previous surveys have been predominantly in single filters—with six filters available, the LSST will be able to naturally perform surface-color, light-curve, and phase-curve studies without the need for follow-up. Across all samples there are fewer observations in the *u* and *y* bands compared to *griz* (see Table 4). The *u* band suffers from survey cadence and object

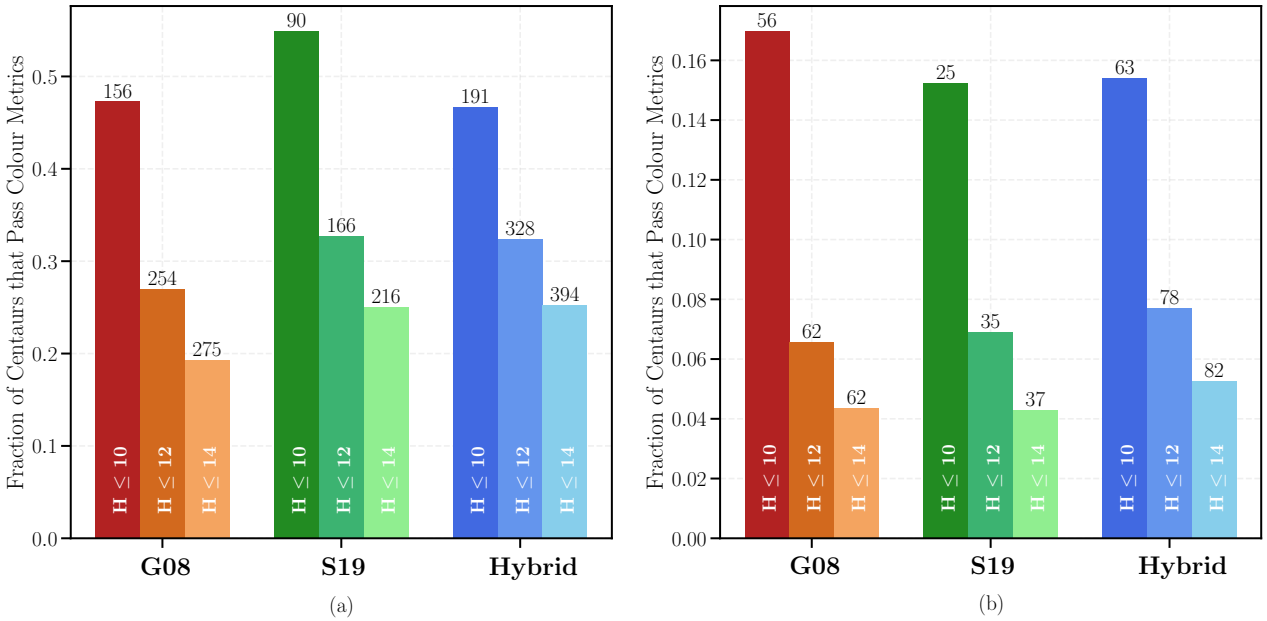

Figure 11. Number of Centaurs that would obtain at least three colors in *ugrizy*. Each bar represents the fraction of each subsample of discovered objects that would pass the color metrics defined in M. E. Schwamb et al. (2023), with the actual number of Centaurs this represents above each bar. Panel (a) highlights those passing the metrics with an S/N $\geqslant$ 5 cut, whereas panel (b) highlights the same but for an S/N $\geqslant$ 25 cut as was used in the OSSOS survey.

colors being fainter in this wavelength range, whereas *y*-band measurements are hindered by survey cadence and near-infrared sky background lowering the limiting magnitude of these observations (F. B. Bianco et al. 2022). For all three samples the median signal-to-noise ratio (S/N) for *griz* measurements is ~8 (or a photometric precision of ~0.125 mag). With ~24 observations per year, the Centaur population will be provided ample opportunities for characterization. In order to probe the quantity and quality of surface colors, light curves, and phase curves that are potentially available within our samples, we look to M. E. Schwamb et al. (2023) and their set of metrics. These metrics, based on LSST Metrics Analysis Frameworks within `rubin_sim` (R. L. Jones et al. 2014), assume at least 30 observations in one filter and 20 in a second filter per object, all at an S/N $\geqslant$ 5. While not a guarantee for precise measurement, these metrics provide a first approximation to determining sparse light curves, as well as fitting phase curves, which will allow for the determination of surface colors.

We apply these metrics in Figure 11, with ~210–400 $H \leqslant 14$ (our sample size decreases for H fainter than this for all three definitions; see Figure 9) Centaurs across the three samples obtaining three colors across *ugrizy*. This is at least an order-of-magnitude increase from the samples used to investigate bimodality in S. C. Tegler & W. Romanishin (1998, 2003; $N = 5, 3$), N. Peixinho et al. (2003; $N = 18$), and I. Wong & M. E. Brown (2016; $N = 15$) and a ~4-fold increase on the S. C. Tegler et al. (2016) studies ($N = 50$). Alternative color studies, such as the Colors of the Outer Solar System Origins Survey (Col-OSSOS; M. E. Schwamb et al. 2019; W. C. Fraser et al. 2023), use a differing threshold of S/N $\geqslant$ 25 in order to create a more precisely measured sample of objects in order to investigate ice-line transitions in the protoplanetary disk. We additionally modify the M. E. Schwamb et al. (2023) metrics to increase the S/N requirement to create a Col-OSSOS quality subsample, shown in Figure 11. With ~40–80 $H \leqslant 14$ Centaurs across the three samples, this massively increases the single Centaur sample size within Col-OSSOS. With such an expanded sample, the origin of Centaurs in the primordial disk will be further able to be probed, as well as investigating the effects of thermal processing on surface colors. Regardless of which metric is used, both results here highlight the LSST's ability to create expanded studies into Centaur evolutionary history, with the potential for ultraprecisely measured surface colors.

Phase curves remain an important method for probing an object's overall surface properties over changing viewing angles. For all three definitions of our objects, we sample a phase-angle range less than ~9°–14°, with the median phase angle at time of discovery being ~2°. The prior metrics will allow for determination of quality phase curves as a by-product of the criteria required for light-curve measurement. We also look at phase-curve-specific quality metrics for our sample in order to determine the density and quality that will be available naturally through the LSST cadence. We fit observations with a linear slope with `curve_fit` from `scipy`, using parameters determined from a Monte Carlo synthetic phase-curve algorithm, trialing 10,000 phase curves within the Gaussian uncertainties of each data point. After fitting, we make a cut on phase-curve quality using a modified set of metrics as initially defined in J. E. Robinson et al. (2024) for Jupiter Trojans, a set of objects also observed in a wide-field survey, albeit with slightly larger phase-angle range behavior. The cuts as listed below allow for removal of observations with poor photometric precision, as well as limiting spread in the data set by placing limits on the phase-curve fit itself. The cuts used are as follows:

(a) The number of photometric points $\geqslant$ 25.
(b) The phase-angle range $\alpha_{\max}$–$\alpha_{\min} \geqslant 3°$.
(c) The absolute magnitude uncertainty $\sigma_H \leqslant 0.1$ mag.
(d) The best-fit linear phase coefficient uncertainty $\sigma_\beta \leqslant 0.02$ mag deg^{-1}.

The overall numbers of phase curves available for each definition are highlighted in Table 5, with an example G08

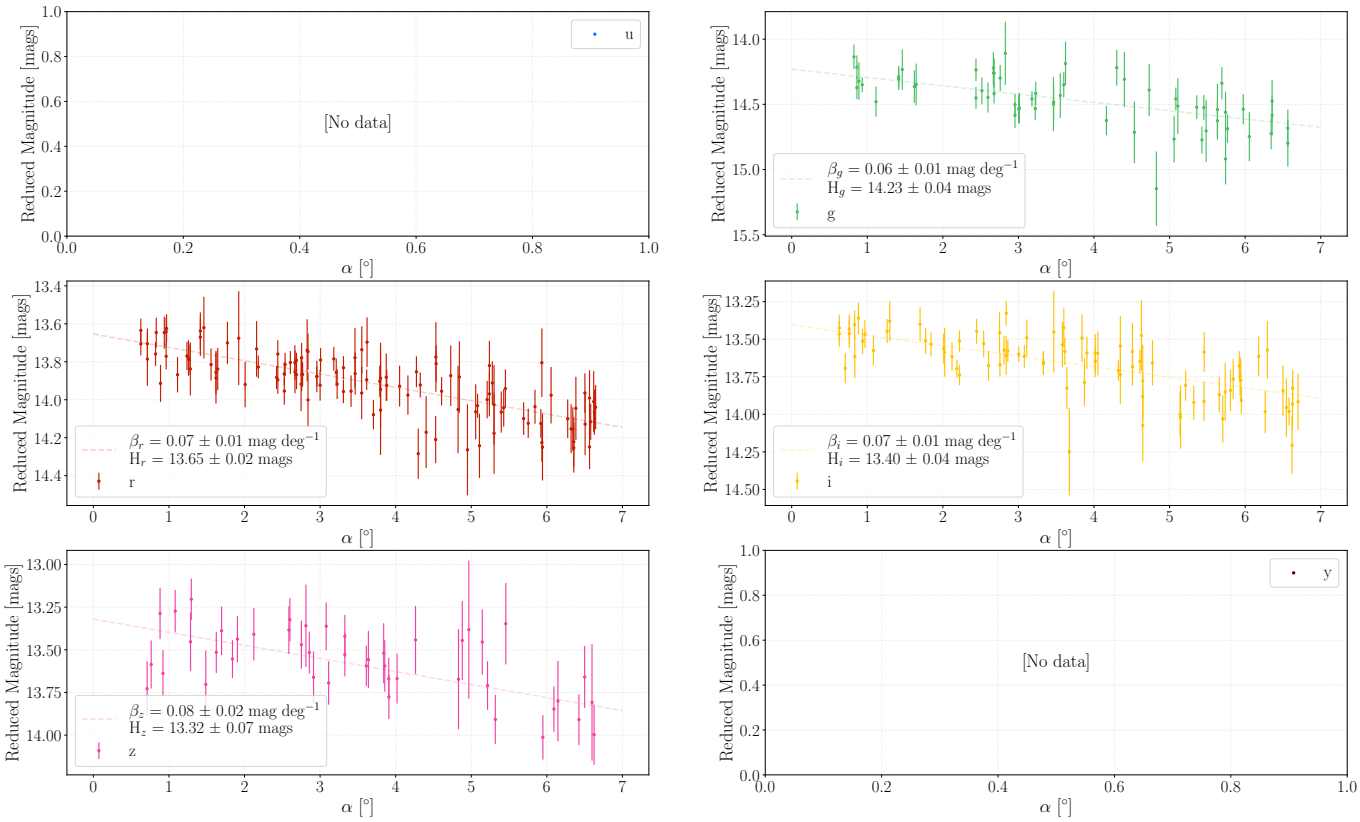

Figure 12. Example phase curves across all *ugrizy* filters for a randomly sampled object from the G08 sample. There are no *uy*-band phase curves here, as they do not have enough observations passing metrics for quality phase curves. All filters that do pass the metrics have been overplotted with the linear fit to the data as determined in the text.

Table 5
Number of High-quality Phase Curves Available per Filter for Each Sample Definition after Applying the Metrics Described in Section 3.4

	# *u*	# *g*	# *r*	# *i*	# *z*	# *y*
G08 sample	34	456	825	755	451	162
S19 sample	12	411	736	663	421	154
Hybrid sample	29	629	1112	990	622	238

object's *ugrizy* phase curves shown in Figure 12. Here we show an order-of-magnitude increase on the 23 Centaurs used in the C. Ayala-Loera et al. (2018), A. Alvarez-Candal et al. (2016), and D. L. Rabinowitz et al. (2007) studies. Comparing the H_r uncertainties with those of the H_V uncertainties reported by the JPL Small Body Database,[19] only ∼80 values have uncertainties, with a median uncertainty of 0.33 mag—our sample of detected objects have median measured uncertainties an order of magnitude lower than this at ∼0.03 mag in the *griz* filters. With ∼9-to-14-fold more absolute magnitude measurements available from *r*-band phase curves alone, the LSST will be capable of massively increasing the sample size of absolute magnitudes of Centaurs currently available.

4. Conclusions

In this work, we have used the current best dynamical model that describes the Centaur population (D. Nesvorný et al. 2019), combined with real, accurate colors and phase-curve parameters in order to investigate the Centaur yield within the LSST. We have also showcased the potential for characterizing them through light-curve and phase-curve analysis. In order to do this, we used the survey simulator `Sorcha` (M. J. Holman et al. 2025; S. R. Merritt et al. 2025) combined with the current latest survey cadence simulations (SCOC 2024) in order to completely forward-bias the output simulated detections. We investigated this for three different subset definitions of Centaurs in order to investigate the impact this will have on discoverability and characterization. Our main conclusions are summarized as follows:

1. Across all three definitions, the predicted yield of Centaur discoveries is set to increase the known MPC population of 215, 186, and 288 Centaurs by ∼7×, giving 1524, 1170, and 1967 discoveries for the G08, S19, and Hybrid samples, respectively. The lower yields for G08 and S19 represent a more stringent dynamical definitional criterion rather than a decrease in discovered objects.
2. The precise color fraction of blue:red objects within the population does not significantly affect this yield or the rate of discovery of Centaurs, even at either extreme end of simulation, varying on the order of $\lesssim 10^1$ discovered Centaurs.
3. Discovery is predicted to happen relatively early—50% population completion is expected to occur within 2 yr of survey operation. The majority of (on average) brighter objects (i.e., $m \leqslant 23$rd magnitude) are discovered within the first year alone, with the remaining years' discoveries

[19] https://ssd.jpl.nasa.gov/tools/sbdb_query.html

being driven by a combination of fainter objects at the limiting magnitudes gaining enough observations to pass linking metrics.

4. The DDF COSMOS presents an exciting and rich opportunity for Centaur characterization. Only ∼30–50 observable Centaurs enter the field, and by spending on average merely 2 months within the DDF, they will receive twice as many observations as that of an object that never enters will have. At ∼500 photometric points, this represents an important means of constructing high-quality, dense phase and light curves for Centaurs for detailed analysis.
5. The median observational arc for the Centaurs approaches the full 10 yr baseline, with a median ∼200 observations per object—or ∼20 per object per year across the *ugrizy* range. This in and of itself represents a key opportunity for discovery of ongoing cometary-like activity by searches for PSF extension or direct coma detection, as well as its monitoring by way of light-curve and phase-curve analysis.
6. Applying color metrics based on the number of and measured S/N of observations, we see upward of ∼200–300 Centaurs with at least three *ugrizy* color measurements to a photometric precision of 0.2 mag, the typical catalog color uncertainty of objects in the literature. Constraining to a larger S/N yields an ultra–well-defined sample of up to ∼40–80 objects.
7. By applying a set of cuts on the data to ensure quality phase curves, ∼300–500 phase curves are available for investigation in the *griz* filters. Fitting these data sets with linear models shows that median uncertainties in the absolute magnitudes determined here are on the order of ∼0.03 mag, almost doubling the current sample of known absolute magnitudes and bringing the uncertainty on these values down by an order of magnitude of what is currently known in the MPC.

Our predictions for the Centaur yield and characterization within the LSST are dependent on the size of the input model population. We have used a model population using the scaling constants from J. A. Kurlander et al. (2025), as this represents the best constrained value in the literature and provides the most realistic model. However, we note that utilizing alternative scaling changes the expected LSST Centaur yield. Employing the OSSOS observationally matched scaling of $N_0 = 21{,}000$ Centaurs with $H_r < 13.7$ from D. Nesvorný et al. (2019) sees a decrease in population size of ∼2% (or ∼177,000 objects) for the G08 model. This in turn results in an identical ∼2% drop in detections (or, ∼30 objects) and other associated light-curve and surface-color metrics. Employing the alternative scaling derived from Jupiter Trojan size distributions from D. Nesvorný et al. (2019) of $N_0 = 15{,}600$ Centaurs with $H_r < 13.7$ results in an even larger drop of ∼33% (or 2.57×10^6 objects), resulting in ∼400 fewer detected objects for the G08 model. The same results are true for the alternative Centaur definitions. Despite this, the maximum variation in discovered objects is only ∼400 objects between the different H distributions. The same result is true of our choice of single power law for the H distribution—with only a <1% effect on the overall detected numbers, this is drowned out by the random variation of ∼5%–8% between runs. With fewer low-H objects, there will be fewer opportunities for detailed light-curve, phase-curve, and surface-color studies, but only on the order of tens of objects. The choice of N_0 scaling, or functional form of H distribution, does not, however, change our overall conclusions. The LSST will still be transformative in the discovery and characterization of Centaurs, increasing on the known ∼300 MPC sample.

This analysis also has the caveat of depending on perfect template generation within the LSST for difference imaging. Regardless of year 1 template generation status, observations will be able to be recovered as the first-year Data Release is shared ∼1 year after operation begins. M. E. Schwamb et al. (2021) and J. E. Robinson et al. (2025) discuss the impact that year 1 template generation has on the observability of small objects, with M. E. Schwamb et al. (2023) investigating several scenarios of observational cadence. Comparing our predictions for the one-snap realization of the v4.0 cadence to the two-snap realization, we see very little variation in the overall trend or numbers of detections and their potential for characterization.

The immense potential in the long baseline, depth, and high cadence of the LSST for Centaur discoverability and characterization is readily apparent in the rapid rate of Centaur discovery, the dense number of observations they acquire, and the photometric precisions that are able to be reached for color and phase-curve measurements. The LSST represents a transformative opportunity to understand the Centaur population's evolution and dynamics through the data gathered within its decade-long operation. Early science, that is, any science possible through and including the first-year data release, especially represents a rich opportunity for future research, including additional follow-up observations for any objects discovered within the first year with supporting ground-based facilities. Due to the quantity and quality of these data, model testing and refinement with survey simulators like `Sorcha` will also be readily available within the first months of operation of the LSST as progressively debiased LSST data sets become available.

Acknowledgments

This work was supported by a LSST Discovery Alliance LINCC Frameworks Incubator grant [2023-SFF-LFI-01-Schwamb]. Support was provided by Schmidt Sciences. J.M. acknowledges support from the Department for the Economy (DfE) Northern Ireland postgraduate studentship scheme and travel support from the STFC for UK participation in LSST through grant ST/S006206/1. M.E.S. and S.R.M. acknowledge support in part from UK Science and Technology Facilities Council (STFC) grants ST/V000691/1 and ST/X001253/1. M.J., P.H.B., and J.A.K. acknowledge the support from the University of Washington College of Arts and Sciences, Department of Astronomy, and the DiRAC Institute. The DiRAC Institute is supported through generous gifts from the Charles and Lisa Simonyi Fund for Arts and Sciences and the Washington Research Foundation. M.J. wishes to acknowledge the support of the Washington Research Foundation Data Science Term Chair fund and the University of Washington Provost's Initiative in Data-Intensive Discovery. J.M and J.A.K. thank the LSST-DA Data Science Fellowship Program, which is funded by LSST-DA, the Brinson Foundation, and the Moore Foundation; their participation in the program has benefited this work. K.V. acknowledges support from NASA (grants 80NSSC23K1169 and 80NSSC23K0886). S.C. and S.E. acknowledge support by the National Science Foundation through award AST-2307570. Any opinions, findings, and

conclusions or recommendations expressed in this material are those of the authors and do not necessarily reflect the views of the National Science Foundation.

This work was also supported via the Preparing for Astrophysics with LSST Program, funded by the Heising Simons Foundation through grant 2021–2975 and administered by Las Cumbres Observatory. This work was supported in part by the LSST Discovery Alliance Enabling Science grants program, the B612 Foundation, the University of Washington's DiRAC (Data-intensive Research in Astrophysics and Cosmology) Institute, the Planetary Society, Karman+, and Breakthrough Listen, Adler Planetarium through generous support of the LSST Solar System Readiness Sprints. Breakthrough Listen is managed by the Breakthrough Initiatives, sponsored by the Breakthrough Prize Foundation (http://www.breakthroughinitiatives.org).

This research has made use of NASA's Astrophysics Data System Bibliographic Services. This research has made use of data and/or services provided by the International Astronomical Union's Minor Planet Center. The SPICE Resource files used in this work are described in C. Acton et al. (2018) and C. H. Acton (1996). Simulations in this paper made use of the REBOUND *N*-body code (H. Rein & S. F. Liu 2012). The simulations were integrated using IAS15, a 15th-order Gauss–Radau integrator (H. Rein & D. S. Spiegel 2015). Some of the results in this paper have been derived using the healpy and HEALPix packages. This work made use of Astropy,[20] a community-developed core Python package and an ecosystem of tools and resources for astronomy (Astropy Collaboration et al. 2013, 2018, 2022).

This material or work is supported in part by the National Science Foundation through Cooperative Agreement AST-1258333 and Cooperative Support Agreement AST-1836783 managed by the Association of Universities for Research in Astronomy (AURA) and the Department of Energy under contract No. DE-AC02-76SF00515 with the SLAC National Accelerator Laboratory managed by Stanford University.

We are grateful for use of the computing resources from the Northern Ireland High Performance Computing (NI-HPC) service funded by EPSRC (EP/T022175). We gratefully acknowledge the support of the Center for Advanced Computing and Modeling, University of Rijeka (Croatia), for providing supercomputing resources at HPC (High Performance Computing) Bura.

We are particularly grateful to Noemí Pinilla-Alonso for providing the original data for the spectra of (5145) Pholus and (54598) Bienor, from which the color analysis of this work was based on. We also thank the anonymous referee for their constructive feedback, which improved this manuscript.

The authors wish to acknowledge the researchers who worked tirelessly to rapidly develop COVID-19 vaccines and subsequent boosters. Without all their efforts, we would not have been able to pursue this work.

Data Access: The software simulator used in this work is available open-source at https://github.com/dirac-institute/Sorcha. The rubin_sim LSST cadence simulation databases are available at https://s3df.slac.stanford.edu/data/rubin/sim-data/.

Software: Sorcha (S. R. Merritt et al. 2025; M. J. Holman et al. 2025), ASSIST (M. J. Holman et al. 2023; H. Rein et al. 2023), Astropy (Astropy Collaboration et al. 2013, 2018), Healpy (A. Zonca et al. 2019; K. M. G'orski et al. 2005), Matplotlib (J. D. Hunter 2007), Numba (S. K. Lam et al. 2015), Numpy (C. R. Harris et al. 2020), Pandas (W. McKinney 2010; The pandas development team 2020), Pooch (L. Uieda et al. 2020), PyTables (PyTables Developers Team 2002), REBOUND (H. Rein & S. F. Liu 2012; H. Rein & D. S. Spiegel 2015), rubin_sim (F. B. Bianco et al. 2022; P. Yoachim et al. 2023), rubin_scheduler (E. Naghib et al. 2019; P. Yoachim et al. 2024), sbpy (M. Mommert et al. 2019), SciPy (P. Virtanen et al. 2020), Spiceypy (A. Annex et al. 2020), sqlite (https://www.sqlite.org/index.html), sqlite3 (https://docs.python.org/3/library/sqlite3.html), tqdm (C. da Costa-Luis et al. 2023), Jupyter Notebook (T. Kluyver et al. 2016), seaborn (M. L. Waskom 2021), CMasher (E. van der Velden 2020).

[20] http://www.astropy.org

ORCID iDs

Joseph Murtagh https://orcid.org/0000-0001-9505-1131
Megan E. Schwamb https://orcid.org/0000-0003-4365-1455
Stephanie R. Merritt https://orcid.org/0000-0001-5930-2829
Pedro H. Bernardinelli https://orcid.org/0000-0003-0743-9422
Jacob A. Kurlander https://orcid.org/0009-0005-5452-0671
Samuel Cornwall https://orcid.org/0000-0002-0672-5104
Mario Jurić https://orcid.org/0000-0003-1996-9252
Grigori Fedorets https://orcid.org/0000-0002-8418-4809
Matthew J. Holman https://orcid.org/0000-0002-1139-4880
Siegfried Eggl https://orcid.org/0000-0002-1398-6302
David Nesvorný https://orcid.org/0000-0002-4547-4301
Kathryn Volk https://orcid.org/0000-0001-8736-236X
R. Lynne Jones https://orcid.org/0000-0001-5916-0031
Peter Yoachim https://orcid.org/0000-0003-2874-6464
Joachim Moeyens https://orcid.org/0000-0001-5820-3925
Jeremy Kubica https://orcid.org/0009-0009-2281-7031
Drew Oldag https://orcid.org/0000-0001-6984-8411
Maxine West https://orcid.org/0009-0003-3171-3118
Colin Orion Chandler https://orcid.org/0000-0001-7335-1715

References

Acton, C., Bachman, N., Semenov, B., & Wright, E. 2018, P&SS, 150, 9
Acton, C. H. 1996, P&SS, 44, 65
Adams, E. R., Gulbis, A. A. S., Elliot, J. L., et al. 2014, AJ, 148, 55
Alvarez-Candal, A., Ayala-Loera, C., Gil-Hutton, R., et al. 2019, MNRAS, 488, 3035
Alvarez-Candal, A., Fornasier, S., Barucci, M. A., de Bergh, C., & Merlin, F. 2008, A&A, 487, 741
Alvarez-Candal, A., Pinilla-Alonso, N., Ortiz, J. L., et al. 2016, A&A, 586, A155
Annex, A., Pearson, B., Seignovert, B., et al. 2020, JOSS, 5, 2050
Annis, J., Soares-Santos, M., Strauss, M. A., et al. 2014, ApJ, 794, 120
Astropy Collaboration, Price-Whelan, A. M., Lim, P. L., et al. 2022, ApJ, 935, 167
Astropy Collaboration, Price-Whelan, A. M., Sipőcz, B. M., et al. 2018, AJ, 156, 123
Astropy Collaboration, Robitaille, T. P., Tollerud, E. J., et al. 2013, A&A, 558, A33
Ayala-Loera, C., Alvarez-Candal, A., Ortiz, J. L., et al. 2018, MNRAS, 481, 1848
Bagnulo, S., Boehnhardt, H., Muinonen, K., et al. 2006, A&A, 450, 1239
Bailey, B. L., & Malhotra, R. 2009, Icar, 203, 155
Bannister, M. T., Gladman, B. J., Kavelaars, J. J., et al. 2018, ApJS, 236, 18
Barkume, K. M., Brown, M. E., & Schaller, E. L. 2008, AJ, 135, 55

Barucci, M. A., Alvarez-Candal, A., Merlin, F., et al. 2011, Icar, 214, 297
Barucci, M. A., Belskaya, I. N., Fulchignoni, M., & Birlan, M. 2005, AJ, 130, 1291
Barucci, M. A., Brown, M. E., Emery, J. P., & Merlin, F. 2008, in The Solar System beyond Neptune, ed. M. A. Barucci et al. (Tucson, AZ: Univ. Arizona Press), 143
Barucci, M. A., & Merlin, F. 2020, in The Trans-Neptunian Solar System, ed. D. Prialnik, M. A. Barucci, & L. Young (Amsterdam: Elsevier), 109
Bauer, J. M., Grav, T., Blauvelt, E., et al. 2013, ApJ, 773, 22
Belskaya, I. N., Levasseur-Regourd, A. C., Shkuratov, Y. G., & Muinonen, K. 2008, in The Solar System beyond Neptune, ed. M. A. Barucci et al. (Tucson, AZ: Univ. Arizona Press), 115
Bernardinelli, P. H., Bernstein, G. M., Sako, M., et al. 2022, ApJS, 258, 41
Bianco, F. B., Ivezić, Ž., Jones, R. L., et al. 2022, ApJS, 258, 1
Brown, M. E. 2012, AREPS, 40, 467
Buie, M. W., Tholen, D. J., & Horne, K. 1992, Icar, 97, 211
Cabral, N., Guilbert-Lepoutre, A., Fraser, W. C., et al. 2019, A&A, 621, A102
Chandler, C. O., Trujillo, C. A., Oldroyd, W. J., et al. 2024, AJ, 167, 156
Chesley, S. R., & Veres, P. 2017, arXiv:1705.06209
Connolly, A. J., Angeli, G. Z., Chandrasekharan, S., et al. 2014, Proc. SPIE, 9150, 915014
da Costa-Luis, C., Larroque, S. K., Altendorf, K., et al. 2023, tqdm: A Fast, Extensible Progress Bar for Python and CLI, v4.66.1, Zenodo, doi:10.5281/zenodo.8233425
Delgado, F., & Reuter, M. A. 2016, Proc. SPIE, 9910, 991013
Delgado, F., Saha, A., & Chandrasekharan, S. 2014, Proc. SPIE, 9150, 915015
Di Sisto, R. P., & Brunini, A. 2007, Icar, 190, 224
Di Sisto, R. P., & Rossignoli, N. L. 2020, CeMDA, 132, 36
Dobson, M. M., Schwamb, M. E., Benecchi, S. D., et al. 2023, PSJ, 4, 75
Dobson, M. M., Schwamb, M. E., Fitzsimmons, A., et al. 2024, PSJ, 5, 165
Dones, L., Brasser, R., Kaib, N., & Rickman, H. 2015, SSRv, 197, 191
Duncan, M., Levison, H., & Dones, L. 2004, in Comets II, ed. M. C. Festou, H. U. Keller, & H. A. Weaver (Tucson, AZ: Univ. Arizona Press), 193
Duncan, M. J., & Levison, H. F. 1997, Sci, 276, 1670
Elliot, J. L., Kern, S. D., Clancy, K. B., et al. 2005, AJ, 129, 1117
Emel'yanenko, V. V., Asher, D. J., & Bailey, M. E. 2005, MNRAS, 361, 1345
Fedorets, G., Granvik, M., Jones, R. L., Jurić, M., & Jedicke, R. 2020, Icar, 338, 113517
Fernández, Y. R., Kelley, M. S., Lamy, P. L., et al. 2013, Icar, 226, 1138
Fornasier, S., Barucci, M. A., de Bergh, C., et al. 2009, A&A, 508, 457
Fornasier, S., Lazzaro, D., Alvarez-Candal, A., et al. 2014, A&A, 568, L11
Fraser, W. C., & Brown, M. E. 2012, ApJ, 749, 33
Fraser, W. C., Brown, M. E., Morbidelli, A., Parker, A., & Batygin, K. 2014, ApJ, 782, 100
Fraser, W. C., Dones, L., Volk, K., Womack, M., & Nesvorný, D. 2022, in Comets III, ed. K. Meech (Tucson, AZ: Univ. Arizona Press), 121
Fraser, W. C., Pike, R. E., Marsset, M., et al. 2023, PSJ, 4, 80
Gladman, B., Marsden, B. G., & Vanlaerhoven, C. 2008, in The Solar System beyond Neptune, ed. M. A. Barucci et al. (Tucson, AZ: Univ. Arizona Press), 43
G'orski, K. M., Hivon, E., Banday, A. J., et al. 2005, ApJ, 622, 759
Grav, T., Mainzer, A. K., & Spahr, T. 2016, AJ, 151, 172
Guilbert, A., Alvarez-Candal, A., Merlin, F., et al. 2009, Icar, 201, 272
Guilbert-Lepoutre, A., Gkotsinas, A., Raymond, S. N., & Nesvorny, D. 2023, ApJ, 942, 92
Guy, L. P., Bechtol, K., Bellm, E., et al. 2024, Rubin Observatory Plans for an Early Science Program, https://rtn-011.lsst.io/
Harris, C. R., Millman, K. J., van der Walt, S. J., et al. 2020, Natur, 585, 357
Holman, M. J., Akmal, A., Farnocchia, D., et al. 2023, PSJ, 4, 69
Holman, M. J., Bernardinelli, P. H., Schwamb, M. E., et al. 2025, AJ, 170, 97
Holman, M. J., & Wisdom, J. 1993, AJ, 105, 1987
Hoover, D. J., Seligman, D. Z., & Payne, M. J. 2022, PSJ, 3, 71
Hsieh, H. H., Fitzsimmons, A., Novaković, B., Denneau, L., & Heinze, A. N. 2021, Icar, 354, 114019
Hunter, J. D. 2007, CSE, 9, 90
Ivezić, Z. & the LSST Science Collaboration 2013, The LSST System Science Requirements Document, LSST Science Requirements Document, Cadence Note LPM-17, http://ls.st/LPM-17
Ivezić, Ž., Kahn, S. M., Tyson, J. A., et al. 2019, ApJ, 873, 111
Jedicke, R., Larsen, J., & Spahr, T. 2002, Asteroids III (University of Arizona Press), 71
Jewitt, D. 2009, AJ, 137, 4296
Jones, R. L., Chesley, S. R., Connolly, A. J., et al. 2009, EM&P, 105, 101
Jones, R. L., Slater, C. T., Moeyens, J., et al. 2018, Icar, 303, 181
Jones, R. L., Yoachim, P., Chandrasekharan, S., et al. 2014, Proc. SPIE, 9149, 91490B
Jones, R. L., Yoachim, P., Ivezic, Z., Neilsen, E. H., & Ribeiro, T. 2020, Survey Strategy and Cadence Choices for the Vera C. Rubin Observatory Legacy Survey of Space and Time (LSST), v1.2, Zenodo, doi:10.5281/zenodo.4048837
Jurić, M., Axelrod, T., Becker, A. C., et al. 2021, LSST Data Products Definition Document, https://lse-163.lsst.io
Jurić, M., Eggl, S., Moeyens, J., & Jones, R. L. 2020, Proposed Modifications to Solar System Processing and Data Products, Cadence Note DMTN-087, https://dmtn-087.lsst.io/
Kareta, T., Volk, K., Noonan, J. W., et al. 2020, RNAAS, 4, 74
Kareta, T., Woodney, L. M., Schambeau, C., et al. 2021, PSJ, 2, 48
Kluyver, T., Ragan-Kelley, B., Pérez, F., et al. 2016, Positioning and Power in Academic Publishing: Players, Agents and Agendas (IOS Press), 87, https://eprints.soton.ac.uk/403913/
Kulyk, I., Korsun, P., Rousselot, P., Afanasiev, V., & Ivanova, O. 2016, Icar, 271, 314
Kurlander, J. A., Holman, M. J., Bernardinelli, P. H., et al. 2025, AJ, 169, 73
Kurucz, R. L. 2005, MSAIS, 8, 189
Lam, S. K., Pitrou, A., & Seibert, S. 2015, in Proc. Second Workshop on the LLVM Compiler Infrastructure in HPC (New York: ACM), 1
Lawler, S. M., Kavelaars, J. J., Alexandersen, M., et al. 2018a, FrASS, 5, 14
Lawler, S. M., Shankman, C., Kavelaars, J. J., et al. 2018b, AJ, 155, 197
Levison, H. F., & Duncan, M. J. 1997, Icar, 127, 13
Lilly, E., Jevčá, P., Schambeau, C., et al. 2024, ApJL, 960, L8
LSST Science Collaboration, Abell, P. A., Allison, J., et al. 2009, arXiv:0912.0201
LSST Science Collaboration, Marshall, P., Anguita, T., et al. 2017, arXiv:1708.04058
Mazzotta Epifani, E., Dotto, E., Ieva, S., et al. 2018, A&A, 620, A93
McKinney, W. 2010, in Proc. 9th Python in Science Conf., ed. S. van der Walt & J. Millman (Austin, TX: SciPy), 56
Merritt, S. R., Fedorets, G., Schwamb, M. E., et al. 2025, AJ, 170, 100
Mommert, M., Kelley, M., de Val-Borro, M., et al. 2019, JOSS, 4, 1426
Myers, J., Jones, R. L., & Axelrod, T. 2013, Moving Object Pipeline System Design Cadence Note LDM-156, https://docushare.lsst.org/docushare/dsweb/Get/LDM-156/LDM-156.pdf
Naghib, E., Yoachim, P., Vanderbei, R. J., Connolly, A. J., & Jones, R. L. 2019, AJ, 157, 151
Nesvorný, D., Vokrouhlický, D., Stern, A. S., et al. 2019, AJ, 158, 132
The pandas development team 2020, pandas-dev/pandas: Pandas, v2.3.0, Zenodo, doi:10.5281/zenodo.3509134
Peixinho, N., Delsanti, A., Guilbert-Lepoutre, A., Gafeira, R., & Lacerda, P. 2012, A&A, 546, A86
Peixinho, N., Doressoundiram, A., Delsanti, A., et al. 2003, A&A, 410, L29
Peixinho, N., Thirouin, A., Tegler, S. C., et al. 2020, in The Trans-Neptunian Solar System, ed. D. Prialnik, M. A. Barucci, & L. Young (Amsterdam: Elsevier), 307
Perna, D., Barucci, M. A., Fornasier, S., et al. 2010, A&A, 510, A53
Petit, J. M., Kavelaars, J. J., Gladman, B., & Loredo, T. 2008, in The Solar System beyond Neptune, ed. M. A. Barucci et al. (Tucson, AZ: Univ. Arizona Press), 71
Prialnik, D. 1992, ApJ, 388, 196
PyTables Developers Team 2002, PyTables: Hierarchical Datasets in Python, https://www.pytables.org/
Rabinowitz, D., Schwamb, M. E., Hadjiyska, E., & Tourtellotte, S. 2012, AJ, 144, 140
Rabinowitz, D. L., Schaefer, B. E., & Tourtellotte, S. W. 2007, AJ, 133, 26
Rein, H., Holman, M., & Akmal, A. 2023, matthewholman/assist: v1.1.1, Zenodo, doi:10.5281/zenodo.7778017
Rein, H., & Liu, S. F. 2012, A&A, 537, A128
Rein, H., & Spiegel, D. S. 2015, MNRAS, 446, 1424
Robinson, J. E., Fitzsimmons, A., Young, D. R., et al. 2024, MNRAS, 531, 304
Robinson, J. E., Schwamb, M. E., Jones, R. L., et al. 2025, ApJS, 279, 9
Rousselot, P., Petit, J. M., Poulet, F., & Sergeev, A. 2005, Icar, 176, 478
Sarid, G., Volk, K., Steckloff, J. K., et al. 2019, ApJL, 883, L25
Schaefer, B. E., Rabinowitz, D. L., & Tourtellotte, S. W. 2009, AJ, 137, 129
Schwamb, M. E., Fraser, W. C., Bannister, M. T., et al. 2019, ApJS, 243, 12
Schwamb, M. E., Jones, R. L., Chesley, S. R., et al. 2018, arXiv:1802.01783
Schwamb, M. E., Jones, R. L., Yoachim, P., et al. 2023, ApJS, 266, 22
Schwamb, M. E., Jurić, M., Bolin, B. T., et al. 2021, RNAAS, 5, 143
SCOC 2022, Survey Cadence Optimization Committee's Phase 1 Recommendations, Cadence Note PSTN-056, https://pstn-053.lsst.io/
SCOC 2023, Survey Cadence Optimization Committee's Phase 2 Recommendations, Cadence Note PSTN-056, https://pstn-055.lsst.io/

SCOC 2024, Survey Cadence Optimization Committee's Phase 3 Recommendations, Cadence Note PSTN-056, https://pstn-056.lsst.io/
Seccull, T., Fraser, W. C., Puzia, T. H., Fitzsimmons, A., & Cupani, G. 2019, AJ, 157, 88
Seligman, D. Z., Kratter, K. M., Levine, W. G., & Jedicke, R. 2021, PSJ, 2, 234
Shankman, C., Gladman, B. J., Kaib, N., Kavelaars, J. J., & Petit, J. M. 2013, ApJL, 764, L2
Shankman, C., Kavelaars, J., Gladman, B. J., et al. 2016, AJ, 151, 31
Shannon, A., Jackson, A. P., Veras, D., & Wyatt, M. 2015, MNRAS, 446, 2059
Sheppard, S. S., Jewitt, D. C., Trujillo, C. A., Brown, M. J. I., & Ashley, M. C. B. 2000, AJ, 120, 2687
Sheppard, S. S., Trujillo, C., & Tholen, D. J. 2016, ApJL, 825, L13
Sheppard, S. S., Udalski, A., Trujillo, C., et al. 2011, AJ, 142, 98
Silsbee, K., & Tremaine, S. 2016, AJ, 152, 103
Solontoi, M., Ivezić, Ž., West, A. A., et al. 2010, Icar, 205, 605
Steckloff, J. K., Sarid, G., Volk, K., et al. 2020, ApJL, 904, L20
Tegler, S. C., Bauer, J. M., Romanishin, W., & Peixinho, N. 2008, in The Solar System beyond Neptune, ed. M. A. Barucci et al. (Tucson, AZ: Univ. Arizona Press), 105
Tegler, S. C., & Romanishin, W. 1998, Natur, 392, 49
Tegler, S. C., & Romanishin, W. 2000, Natur, 407, 979
Tegler, S. C., & Romanishin, W. 2003, Icar, 161, 181
Tegler, S. C., Romanishin, W., & Consolmagno, G. J. J. S. 2016, AJ, 152, 210
Tiscareno, M. S., & Malhotra, R. 2003, AJ, 126, 3122
Trujillo, C. A. 2008, in The Solar System beyond Neptune, ed. M. A. Barucci et al. (Tucson, AZ: Univ. Arizona Press), 573
Uieda, L., Soler, S., Rampin, R., et al. 2020, JOSS, 5, 1943
van der Velden, E. 2020, JOSS, 5, 2004
Verbiscer, A. J., Helfenstein, P., & Buratti, B. J. 2013, in The Science of Solar System Ices, ed. M. S. Gudipati & J. Castillo-Rogez (Berlin: Springer), 47
Vereš, P., & Chesley, S. R. 2017, AJ, 154, 13
Virtanen, P., Gommers, R., Oliphant, T. E., et al. 2020, NatMe, 17, 261
Volk, K., & Malhotra, R. 2008, ApJ, 687, 714
Volk, K., & Van Laerhoven, C. 2024, RNAAS, 8, 36
Waskom, M. L. 2021, JOSS, 6, 3021
Weryk, R. J., Lilly, E., Chastel, S., et al. 2016, arXiv:1607.04895
Wong, I., & Brown, M. E. 2016, AJ, 152, 90
Wong, I., & Brown, M. E. 2017, AJ, 153, 145
Yoachim, P., Coughlin, M., Angeli, G. Z., et al. 2016, Proc. SPIE, 9910, 99101A
Yoachim, P., Jones, L., Eric, H., Neilsen, J., et al. 2023, lsst/rubin_sim: v2.0.0, Zenodo, doi:10.5281/zenodo.10215451
Yoachim, P., Jones, L., Eric, H., Neilsen, J., et al. 2024, lsst/rubin_scheduler: v3.4.0, Zenodo, doi:10.5281/zenodo.14232232
Zonca, A., Singer, L., Lenz, D., et al. 2019, JOSS, 4, 1298